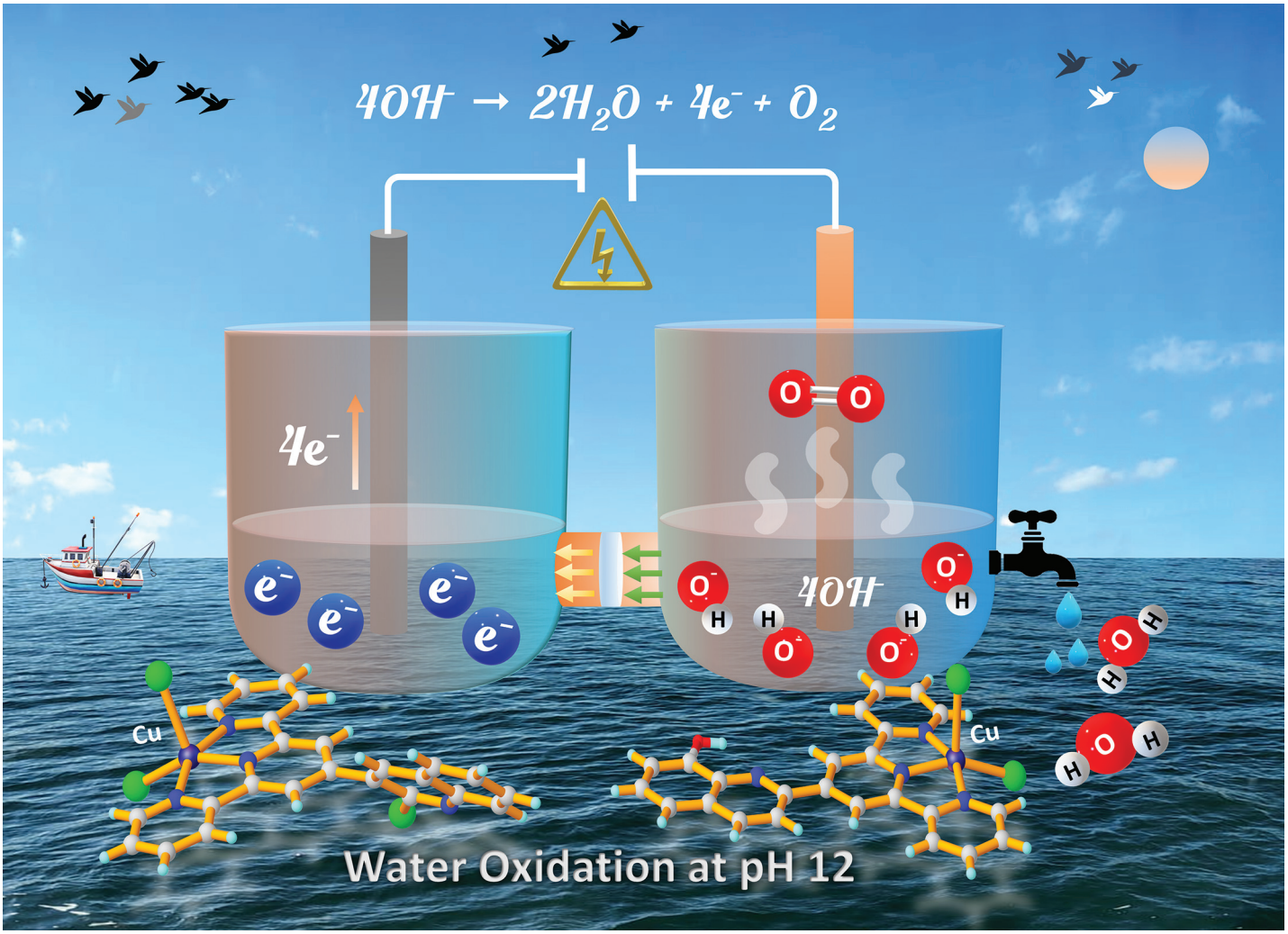

Showcasing research from Professor Sumanta Kumar Padhi's laboratory, Department of Chemistry and Chemical Biology, IIT(ISM) Dhanbad, Jharkhand, INDIA.

Electrochemical water oxidation using single-site Cu(II) molecular complexes: a mechanism elucidated by computational studies

Two penta-coordinated Cu(II) complexes were investigated as electrocatalysts for water oxidation in phosphate buffer (pH 12): [Cu(QCl-Tpy)Cl_2] (QCl-Tpy = 3-([2,2′:6′,2″-terpyridin]-4′-yl)-2-chloroquinoline) and [Cu(8HQ-Tpy)Cl_2] (8HQ-Tpy = 2-([2,2′:6′,2″-terpyridin]-4′-yl)quinolin-8-ol). Both follow a Water Nucleophilic Attack (WNA) pathway with first-order kinetics, where O–O bond formation is made possible by buffer-assisted proton transfer. TOF_{max} values of 10 000 s^{-1} and 15 000 s^{-1} were found using Foot of the Wave Analysis; Tafel plots verified the latter's higher activity. According to theoretical research, WNA is supported, and oxygen evolution is more advantageous in alkaline environments because of hydroxide nucleophilicity.

Image reproduced by permission of Sumanta Kumar Padhi from *Dalton Trans.*, 2025, **54**, 13894.

As featured in:

See Sumanta Kumar Padhi *et al.*, *Dalton Trans.*, 2025, **54**, 13894.

ROYAL SOCIETY OF CHEMISTRY

rsc.li/dalton

Registered charity number: 207890

Dalton Transactions

ROYAL SOCIETY OF CHEMISTRY

PAPER

View Article Online
View Journal | View Issue

Cite this: *Dalton Trans.*, 2025, **54**, 13894

Electrochemical water oxidation using single-site Cu(II) molecular complexes: a mechanism elucidated by computational studies

Dev Raj,[a] Koushik Makhal,[b] Manaswini Raj,[a] Aman Mishra,[a] Rohan Mahapatra,[a] Tanya Pattnaik,[a] Bhabani S. Mallik [b] and Sumanta Kumar Padhi *[a]

In this work, the penta-coordinated mononuclear Cu(II) complexes [Cu(QCl-Tpy)Cl_2], **[Cu1]** (where QCl-Tpy = 3-([2,2′:6′,2″-terpyridin]-4′-yl)-2-chloroquinoline) and [Cu(8HQ-Tpy)Cl_2], **[Cu2]** (where 8HQ-Tpy = 2-([2,2′:6′,2″-terpyridin]-4′-yl)quinolin-8-ol) were utilized as electrocatalysts for water oxidation in 0.1 M $H_2PO_4^-/HPO_4^{2-}$ buffered solution at pH = 12.0. Detailed electrochemical measurements suggest that both complexes follow first-order kinetics and liberate oxygen *via* the water nucleophilic attack (WNA) pathway. The active participation of the buffer under electrochemical conditions indicates its strong atom proton transfer (APT) ability, thereby facilitating the O–O bond formation. The TOF and TOF_{max} of the catalysts were elucidated using foot-of-the-wave analysis (FOWA) and catalytic Tafel plot. The complexes **[Cu1]** and **[Cu2]** exhibit TOF_{max} values of 10 × 10^3 s^{-1} and 15 × 10^3 s^{-1}, respectively, as elucidated by FOWA, assuming a first-order rate constant. The catalytic Tafel plot supports the superior electrocatalytic activity of the catalyst **[Cu2]** in contrast to catalyst **[Cu1]**. Theoretical studies also affirm that both catalysts undergo WNA and thereby follow first-order kinetics. Moreover, theoretical studies demonstrate that the oxygen evolution reaction (OER) is thermodynamically more favourable at higher alkaline pH owing to the better nucleophilicity of the hydroxide ions.

Received 13th June 2025,
Accepted 15th August 2025

DOI: 10.1039/d5dt01397f

rsc.li/dalton

Introduction

A new research domain where solar energy is captured and stored in chemical bonds through artificial photosynthesis has intrigued researchers[1] as it provides an accessible pathway for the generation of fuels such as hydrogen and hydrocarbons.[2] In the context of artificial photosynthesis, water oxidation is an instrumental reaction as four protons and four electrons are consequently released, which is necessary for O=O bond formation.[3]

$$2H_2O \rightarrow O_2 + 4H^+ + 4e^-;$$
$$E^{\circ}_{H_2O} = +1.23\,V\ vs.\ NHE,\ pH = 0$$

Depending upon the pH of the aqueous media, oxygen liberation occurs by splitting water into two different half-reactions (Scheme 1). In acidic pH (pH = 0.0), protons are formed at the anode, followed by simultaneous generation of O_2 gas upon oxidizing water. These generated protons act as charge carriers and get reduced to H_2 gas at the cathode. Meanwhile, in alkaline pH (pH = 14.0), the hydroxyl ions formed at the cathode due to water reduction act as an electrochemical charge carrier, which gets oxidized at the anode to liberate O_2 gas.[4a,b] The large scale generation of O_2 *via* water splitting using molecular catalysts has not been fully explored due to sluggish reaction kinetics.[5] Hence, a stable and robust molecular catalyst is essential for water oxidation, as tuning ligand design can modulate the electronic structure and catalytic properties, enabling high catalytic rates with minimal overpotential.[6] Mn_4CaO_5, being a natural oxygen-evolving complex of

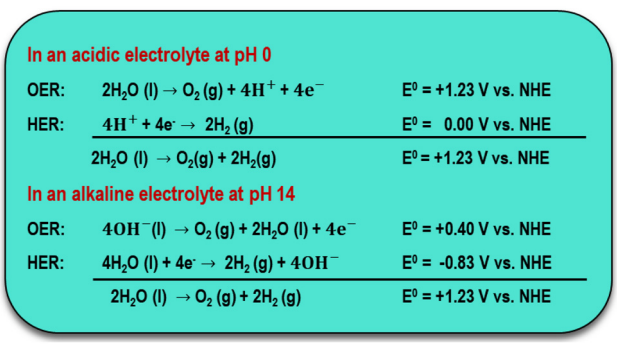

Scheme 1 Water splitting half-reaction at acidic and alkaline pH.

[a]*Artificial Photosynthesis Laboratory, Department of Chemistry and Chemical Biology, Indian Institute of Technology (Indian School of Mines), Dhanbad, 826004, India. E-mail: sumanta@iitism.ac.in*
[b]*Department of Chemistry, Indian Institute of Technology Hyderabad, Sangareddy, 502284 Telangana, India*

Photosystem II, produces oxygen along with the release of protons and electrons.[7,8] Hence, the ultimate goal in the design of water oxidation catalysts (WOCs) is to develop a molecular catalyst that will be comparable with the natural photosynthetic cluster $CaMn_4O_5$ in water-splitting efficiency.

Primarily, O–O bond formation takes place *via* two possible mechanistic pathways: water nucleophilic attack (WNA)[9] and interaction of two metal-oxo entities (I2M).[10] However, various groups have further suggested that oxygen evolution might also go through a redox isomerization process (RI) and will only be noted when there exists μ-oxo linkages between the bimetallic centres.[11] Of the several homogeneous catalysts, the Ru[12a–h] and Ir[13a,b]-based WOCs reported by various research groups act as a promising catalyst for water oxidation. However, their mass usage had been limited as these catalysts possess a huge economic burden. Therefore, the use of WOCs based on non-precious metals such as Mn,[14] Fe,[15] Co,[16] Ni[17] and Cu[18] has increased, offering a sustainable alternative to precious metals. Among these late first-row transition metal complexes, extensive research had been carried out for an electrochemical water oxidation (WO) using Cu-based catalysts,[19a,b] owing to their diverse biomimetic coordination chemistry and its presence at the active sites of various metalloenzymes.[20] Moreover, in the foremost report of a Cu-based molecular WOC derived from a copper-bipyridine complex,[21] numerous Cu catalysts had been enumerated as oxygen evolving complexes with simple Cu(II) salts.[22a,b] A diverse range of ligands with multi-denticity had been incorporated in the design of molecular Cu WOCs,[23a,b] where a modest alteration in the ligand framework minimizes the overpotential by more than 200 mV under alkaline pH, signifying the prominent role of the ligand.[24] Llobet *et al.* had reported on various Cu-based electrocatalysts for WO using various substituted tetradentate amidate ligands based on N_1,N'_1-(1,2-phenylene)bis(N_2-methyl-oxalamide). Electrochemical measurements confirm the formation of a $Cu^{III/II}$ redox couple at $E_{1/2}$ = 0.56 V *vs.* NHE, where the configuration around the metal centre remains square planar with infinitesimal change in the reorganizational energy. DFT studies confirm that catalysts follow the SET-WNA pathway, through which a radical cation is formed and further undergoes reaction with OH^- ions. The overpotential of the complexes gets drastically reduced to 150 mV when the ligand moiety gets substituted by electron-donating groups.[25] The oxygen evolution was further examined using a [Cu(pimH)] catalyst {where pimH = 2-(2′-pyridyl)-imidazole} at various pH values ranging from pH = 8.0 to 12.0. The catalyst follows first-order kinetics and exhibits a TOF value of 35 s^{-1}. The presence of an ionizable imidazole moiety stabilizes the metal centre in a higher oxidation state. Consequently, the overpotential of the complex is lowered to 300 mV.[26] At neutral pH in 0.1 M phosphate buffer, Cao *et al.* reported that the [Cu-porphyrin] {porphyrin = tetrakis(4-*N*-methylpyridyl)porphyrin} catalyst possesses a remarkable water splitting property and oxidizes water at an overpotential of 310 mV. The catalyst exhibits a faradaic efficiency of 93% upon performing controlled potential electrolysis using a FTO working electrode for 10 hours at E° = 1.30 V *vs.* NHE.[27] Sun and co-workers reported on two Cu-based electrocatalysts which oxidized water in 0.1 M phosphate buffered saline (PBS) at pH = 11.50. Electrochemical measurements indicate that the catalytic peak potential varies with a gradual increment of pH from 9.0 to 12.50. The complexes undergo WNA and manifest a TOF of 13.1 s^{-1} and 18.7 s^{-1}.[28] Zhang *et al.* reported on a water-soluble Cu-based electrocatalyst [Cu(N_2Py_3)] {where N_2Py_3 = 2,6-bis[(methyl(2-pyridylmethyl)amino)methyl]pyridine} for oxygen evolution at pH = 11.0 in phosphate buffer. Cyclic voltammetry studies indicate that the electrocatalyst exhibits a reversible $Cu^{II/I}$ redox peak at $E_{1/2}$ = −0.11 V *vs.* NHE. The complex follows first-order kinetics and undergoes atom proton transfer (APT) with the increment of the phosphate buffer concentration from 25.0 mM to 100.0 mM.[29] Kalita *et al.* reported that [Cu(L_1H)(L_1)(OH_2)] {L_1H = 1-(pyridin-2-yl) ethanone oxime} acts as a robust catalyst for the electrochemical evolution of oxygen in phosphate buffer at pH = 7.0. Redox studies indicate that the complex exhibits $Cu^{II/I}$ and $Cu^{III/II}$ redox peaks at E° = −0.09 V *vs.* Ag/AgCl and E° = 0.64 V *vs.* Ag/AgCl, respectively. CPE at E° = 1.55 V *vs.* NHE for 4 hours demonstrated oxygen evolution with a faradaic efficiency of 94% using an ITO working electrode.[30]

In this study, the usage of two monomeric Cu(II) complexes [Cu(QCl-Tpy)Cl_2]; **[Cu1]** (where QCl-Tpy = 3-([2,2′:6′,2″-terpyridin]-4′-yl)-2-chloroquinoline) and [Cu(8HQ-Tpy)Cl_2]; **[Cu2]** (where 8HQ-Tpy = 2-([2,2′:6′,2″-terpyridin]-4′-yl)quinolin-8-ol) supported on terpyridine moiety were demonstrated as stable water oxidation electrocatalysts in 0.1 M $H_2PO_4^-/HPO_4^{2-}$ buffered solutions at pH = 12.0. Electrochemical measurements supported by experimental and density functional theory (DFT) studies provide evidence for a single-site water oxidation mechanism involving an atom proton transfer (APT) step.

Experimental section

Synthesis of the [Cu(QCl-Tpy)Cl_2]; [Cu1]

A methanolic solution of 0.34 mmol of $CuCl_2{\cdot}2H_2O$ was incorporated into a solution mixture of DCM and MeOH (4 : 1; v/v) consisting of ligand QCl-Tpy (0.34 mmol), and allowed to stir at room temperature for 4 hours (Scheme 2a). The excess solution was removed by vacuum evaporation and the obtained residue was dissolved in a mixture of MeOH : Et_2O (1 : 10 v/v). Upon filtration followed by vacuum drying, a light green precipitate of **[Cu1]** was obtained. Light green crystals of the **[Cu1]** complex that were suitable for crystallography were obtained in a MeOH medium after several weeks. Calculated mass for $[Cu(C_{24}H_{15}ClN_4)Cl]^+$ m/z = 494.0069; obtained m/z = 494.0014. Elemental analysis for [Cu(QCl-Tpy)Cl_2] [Cu($C_{24}H_{15}ClN_4$)Cl_2]; C, 54.46%; H, 2.86% and N, 10.56% and found C, 54.61%; H, 2.93% and N, 10.59%.

[Cu(8HQ-Tpy)Cl_2]; [Cu2]

Under room temperature, a 1 : 1 mixture of $CuCl_2{\cdot}2H_2O$ (0.34 mmol) and 8HQ-Tpy (0.34 mmol) was incorporated into a solution mixture of DCM : MeOH (4 : 1 v/v), and formed a greenish yellow precipitate when the resulting solution was allowed to stir for 4 hours (Scheme 2b). The obtained precipitate was filtered, washed continuously with chilled Et_2O and

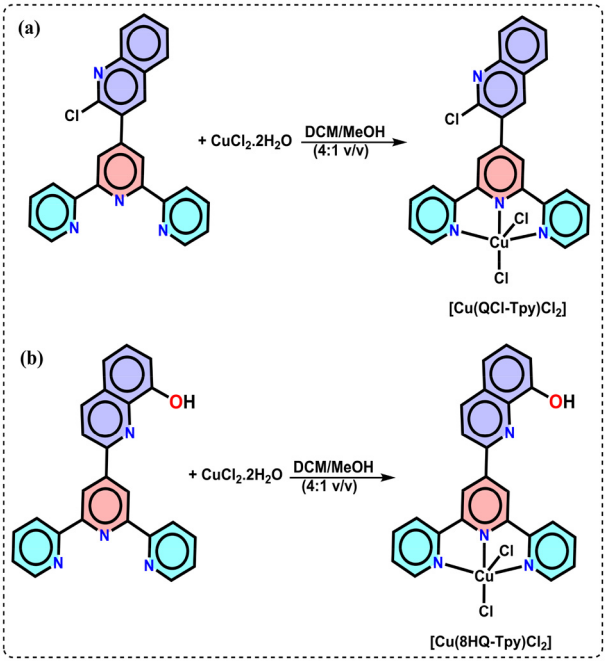

Scheme 2 Synthetic route of (a) [Cu(QCl-Tpy)Cl_2]; **[Cu1]** and (b) [Cu(8HQ-Tpy)Cl_2]; **[Cu2]**.

kept for vacuum drying. The dried product was further recrystallized using DMF, thereby yielding greenish-yellow crystals of complex **[Cu2]**. Calculated mass for $[Cu(C_{24}H_{16}ON_4)Cl]^+$ m/z = 474.0408; obtained m/z = 474.0400. Elemental analysis for [Cu(8HQ-Tpy)Cl_2] [Cu($C_{24}H_{16}ON_4$)Cl_2]; C, 56.43%; H, 3.16% and N, 10.97% and found C, 56.47%; H, 3.17% and N, 10.99%.

Results and discussion

The ligands QCl-Tpy and 8HQ-Tpy were synthesized according to the synthetic procedure reported in the literature.[31,32] Upon dissolution of one equivalent of ligand QCl-Tpy into a solvent mixture of DCM : MeOH (4 : 1 v/v), one equivalent of $CuCl_2{\cdot}2H_2O$ was incorporated and stirred at room temperature for 4 hours. The resulting light green precipitate of **[Cu1]** was filtered, and washed with MeOH and Et_2O. The obtained precipitate of **[Cu1]** was vacuum dried and dissolved in MeOH. Upon slow evaporation, the solution yields light green crystals of the **[Cu1]** complex. The greenish-yellow precipitate was formed upon addition of one equivalent of $CuCl_2{\cdot}2H_2O$ to a solvent mixture of DCM : MeOH (4 : 1 v/v) consisting of one equivalent of the ligand 8HQ-Tpy. The obtained precipitate was filtered and washed with Et_2O. Slow evaporation of DMF produced greenish-yellow crystals of complex **[Cu2]**. The NMR spectra of the ligands QCl-Tpy and 8HQ-Tpy are shown in Fig. S1–S4, while the FTIR spectra of the ligands and their complexes are presented in Fig. S5–S6.

Absorption spectra

The electronic absorption spectra of both copper complexes, **[Cu1]** and **[Cu2]**, had been examined in the organic solvent *N*,*N*-dimethyl formamide.[33a] The complex **[Cu1]** exhibits a broad low intensity band at λ_{max} = 732 nm (ε = 83.0 M^{-1} cm^{-1}). Additionally, complex **[Cu1]** exhibits a band at λ_{max} = 573 nm (ε = 49.0 M^{-1} cm^{-1}), illustrating that it undergoes Jahn–Teller distortion between the $^2B_1$ to ^2E energy states. Two peaks for the ligand QCl-Tpy had been noted at λ_{max} = 280 nm (ε = 12944.0 M^{-1} cm^{-1}) and at λ_{max} = 320 nm (ε = 4753.0 M^{-1} cm^{-1}) due to π–π* and n–π* transitions, respectively (Fig. S7a). Due to the electron-donating ability of the ligand 8HQ-Tpy, a bathochromic shift was noted in the complex **[Cu2]**. A metal-based peak at λ_{max} = 760 nm (ε = 106.0 M^{-1} cm^{-1}) was observed, along with a small intensity band at λ_{max} = 595 nm (ε = 89.0 M^{-1} cm^{-1}), illustrating that it undergoes Jahn–Teller distortion. These transitions were mainly attributed to the square pyramidal geometry of the complexes, which undergoes transitions from $^2B_1$ to $^2A_1$ and $^2B_1$ to ^2E energy states (Fig. S7c).[33b] The ligand 8HQ-Tpy also shows a peak at λ_{max} = 280 nm (ε = 25476.0 M^{-1} cm^{-1}) due to a π–π* transition, and another at λ_{max} = 325 nm (ε = 6915.0 M^{-1} cm^{-1}) corresponding to the n–π* transition (Fig. S7b). The low molar extinction coefficient value for the n–π* transition in contrast to π–π* transition was attributed to the anti-symmetric nature of the transition moment integral.

Mass spectra

The composition of both ligands and complexes had been determined by mass spectrometry in DCM and aqueous medium, respectively. The protonated QCl-Tpy ligand exhibits a molecular ion peak at 395.1049 [M + H^+] (with M representing $C_{24}H_{15}N_4Cl$), whereas the simulated value corresponds to 395.1058 (Fig. S8). The peak at 494.0015 m/z is attributed to $[C_{24}H_{15}N_4Cl_2Cu]^+$ [Cu(QCl-Tpy)Cl]$^+$ for the **[Cu1]** complex (Fig. S9). Moreover, the ligand 8HQ-Tpy manifests a molecular ion peak at 377.1377 [M + H^+] (where M represents $C_{24}H_{16}N_4O$), whereas the predicted value was illustrated to be at 377.1396 (Fig. S10). The **[Cu2]** complex exhibits a peak at 474.0400 m/z corresponding to $[C_{24}H_{16}N_4OClCu]^+$ [Cu(8HQ-Tpy)Cl]$^+$ (Fig. S11). The mass spectra of the complexes demonstrate that one of the chlorides was labile in the solution phase.

Single crystal X-ray structure

The catalyst [Cu(QCl-Tpy)Cl_2] **[Cu1]** crystallizes in the monoclinic $P2_1/n$ space group. The overall complex was neutral and mononuclear, comprising an asymmetric unit of the complex [Cu(QCl-Tpy)Cl_2] and a MeOH molecule as the solvent of crystallization. The Cu metal center was pentacoordinated in the [Cu(QCl-Tpy)Cl_2] complex, as displayed in the Oak Ridge thermal ellipsoid plot (ORTEP) (Fig. 1a). The crystal data and refinement parameters are listed in Tables S1–S3. Complexes possessing pentacoordinated geometry can have two possible structures, trigonal bipyramidal (tbp) or square pyramidal (spy). At the **[Cu1]** metal center, α = 151.62°, β = 155.53° and τ_5 = 0.06, thereby indicating a square pyramidal geometry at the Cu-center (Fig. 1c). This can be attributed to the structural

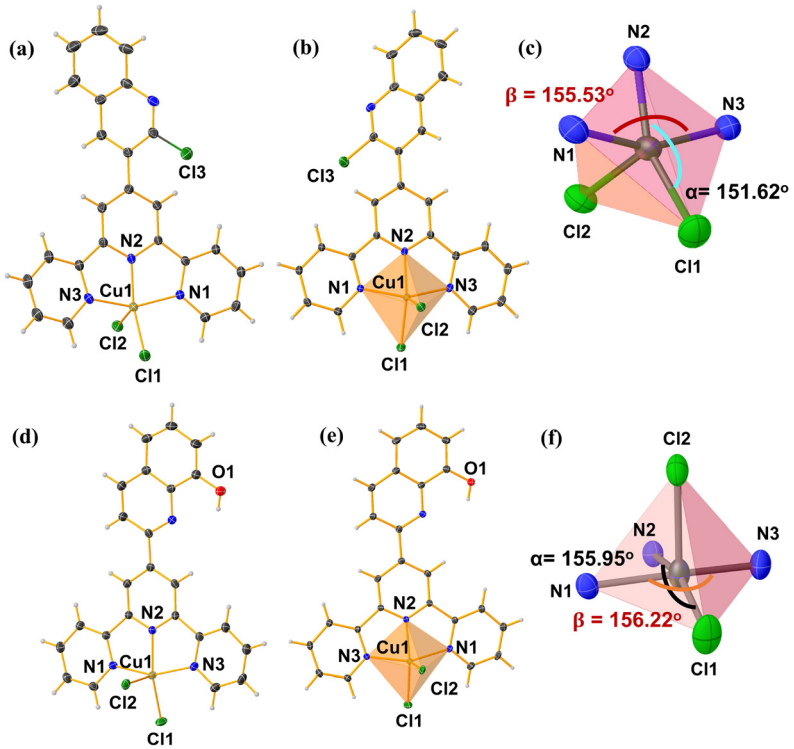

Fig. 1 (a) ORTEP of complex [Cu(QCl-Tpy)Cl_2]; **[Cu1]** MeOH molecule has been removed for clarity. (b) Five-coordinated polyhedron of **[Cu1]**. (c) Structural parameters in the square pyramidal geometry of **[Cu1]**. (d) ORTEP of [Cu(8HQ-Tpy)Cl_2]; **[Cu2]** DMF molecule has been removed for clarity. (e) Five-coordinated polyhedron of **[Cu2]**. (f) Structural parameters in the square pyramidal geometry of **[Cu2]**.

parameter (τ_5) from the penta-coordinated geometry calculated by means of eqn (1):

$$\tau_5 = \frac{\beta - \alpha}{60^\circ} \approx -1.01667\alpha + 1.01667\beta \quad (1)$$

The Cu-center of the [Cu(QCl-Tpy)Cl_2] catalyst had a square pyramidal geometry, wherein the square-plane consists of N1, N2, N3 and Cl1 as the coordinating atoms. The Cl2 atom occupies the apical position. Moreover, the Cu–N neutral coordination was stronger and shorter than the Cu–Cl anionic coordination. It had been noted that the *trans*-coordinating Cu–N_{py} bonds (2.043 Å and 2.045 Å) were longer than the Cu–N_{py} (central) bond (1.938 Å) owing to the overlap of the π*-orbital of the central pyridine ring with the Cu-t_{2g} orbital. The bite angles generated by ∠N(2)Cu(1)N(1) and ∠N(2)Cu(1)N(3) at 78.66° and 78.38°, respectively, deviate considerably from a right angle. The angles generated due to the *trans* coordinating atoms ∠N(1)Cu(1)N(3) (155.53°) and ∠N(2)Cu(1)Cl(1) (151.62°) strongly deviate from linearity. The mononuclear complex [Cu(8HQ-Tpy)Cl_2] **[Cu2]** crystallizes in a triclinic $P\bar{1}$ space group with the asymmetric unit of the complex consisting of a neutral [Cu(8HQ-Tpy)Cl_2] moiety and dimethyl formamide as the solvent for crystallization. The pentacoordinated Cu metal center adopts a distorted square pyramidal geometry as evidenced by eqn (1), where the structural parameter (τ_5) has been calculated to be 0.0045 (α = 155.95°, β = 156.22°). The equatorial plane comprises three N_{tpy} atoms (N1, N2 & N3) and Cl1 atoms, whereas the apical position was occupied by the Cl2 atom as represented in ORTEP (Fig. 1d).

The crystal data and refinement parameters are listed in Tables S4–S6. As a consequence of the overlap of the π*-orbital of the central pyridine ring with the Cu-t_{2g} orbital, the Cu–N_{py} (central) bond (1.965 Å) was comparatively shorter than the *trans*-coordinating Cu–N_{py} bonds (2.050 Å and 2.040 Å). Furthermore, the Cu–Cl2 apical bond (2.4942 Å) was comparatively longer than the Cu–Cl1 bond (2.2428 Å). The bite angles generated by ∠N(2)Cu(1)N(1) and ∠N(2)Cu(1)N(3) at 78.69° and 78.71°, respectively, deviate considerably from a right angle. The angles generated due to the *trans* coordinating atoms ∠N(1)Cu(1)N(3) (156.22°) and ∠N(2)Cu(1)Cl(1) (155.95°) strongly deviate from linearity. Significant π···π stacking interactions are observed between the Tpy ligands in complexes **[Cu1]** and **[Cu2]**, with centroid–centroid distances of 3.736 Å and 3.741 Å, respectively (Fig. S12).

Solution phase magnetic properties

The Evans Method was used to calculate the effective magnetic moment (μ_{eff}) of complexes **[Cu1]** and **[Cu2]** in a solution comprising DMSO and 10% ^{t}BuOH, and its ^{1}H NMR spectra were recorded at room temperature. The effective magnetic moment (μ_{eff}) of both complexes **[Cu1]** and **[Cu2]** stands out at 2.0534μ_B and 1.910μ_B, respectively (Fig. S13). It infers the presence of only one unpaired electron in the metal center of both complexes and further confirms their mononuclear nature.[34,35] The detailed calculations are provided in the SI.

Solid-state magnetic properties

The complexes **[Cu1]** and **[Cu2]** were studied for their solid-state magnetic characteristics at 1000 Oe throughout the temperature range of 10–300 K. Complexes **[Cu1]** and **[Cu2]** have χT values of 0.48 and 0.49 cm^3 K mol^{-1} at 300 K, respectively (where χ is the molar susceptibility). As the temperature drops, the χT value drops linearly in the case of **[Cu1]** (Fig. S14(A)). The presence of an antiferromagnetic interaction is indicated by this behaviour in **[Cu1]**.[36] However, it is different in the case of the complex **[Cu2]** (Fig. S14(B)). The χ^{-1} *vs.* T plots in the complexes **[Cu1]** and **[Cu2]** do not follow a linear plot. The presence of the curvature is usually observed due to the temperature-independent magnetic susceptibility. In order to obtain the best-fit parameters, the modified Curie–Weiss law was fitted to the data, following eqn (2a) and (2b). In the case of **[Cu1]**, the Neil temperature (θ_{CW}) was −0.82 ± 0.01 K, along with the Curie–Weiss constant of 0.15 ± 0.01.36. The temperature-independent magnetic susceptibility χ_0 in **[Cu1]** was calculated to be 1.12 × 10^{-3} cm^3 mol^{-1}. But for **[Cu2]**, the Curie temperature, θ_{CW}, was +8.32 K, and the Curie constant was 0.08 ± 0.01 for the fitting range of 10–250 K (Fig. 2). The temperature-independent magnetic susceptibility χ_0 in **[Cu2]** was found to be 1.17 × 10^{-3} cm^3 mol^{-1}.

$$\chi = \frac{C}{T - \theta_{CW}} + \chi_0 \quad (2a)$$

$$\chi^{-1} = \frac{T - \theta_{CW}}{\chi_0 (T - \theta_{CW})} + C \quad (2b)$$

Electrochemistry

The cyclic voltammogram of complex **[Cu1]** in DMF exhibits a metal-based irreversible peak at $E_{p,c}$ = −0.156 V and $E_{p,a}$ = −0.046 V *vs.* SCE for the $Cu^{0/I}$ redox couple (Fig. 3a). Another peak corresponding to the $Cu^{I/II}$ redox couple had an $E_{1/2}$ = 0.381 V *vs.* SCE ($E_{p,c}$ = 0.333 V and $E_{p,a}$ = 0.428 V *vs.* SCE) and an irreversible nature.[37a–d] On the other hand, ligand QCl-Tpy exhibits two cathodic peaks at −1.652 V and −1.772 V *vs.* SCE. Besides these, several anodic peaks had been noted with the most prominent being a peak at $E_{p,a}$ = 1.06 V *vs.* SCE (Fig. S15a & S15b).[38]

Upon performing CV under similar electrochemical conditions in DMF medium, two quasi-reversible peaks at $E_{1/2}$ = −0.106 V *vs.* SCE for the $Cu^{0/I}$ redox species and at $E_{1/2}$ = 0.415 V ($E_{p,c}$ = 0.355 V and $E_{p,a}$ = 0.475 V *vs.* SCE) for the $Cu^{I/II}$ redox couples, respectively, had been noted for complex **[Cu2]** (Fig. 3b), whereas the ligand 8HQ-Tpy exhibits two irreversible peaks at E = −1.528 V *vs.* SCE and at E = −1.875 V *vs.* SCE (Fig. S15c and S15d).[39] Furthermore, it had been observed that the ligand 8HQ-Tpy displays several anodic peaks with the notable one being peak at $E_{p,a}$ = 1.11 V *vs.* SCE (Fig. S15c). The anodic shift in the ligand-based redox peaks of the complex to a high positive potential, in contrast to the ligands QCl-Tpy and 8HQ-Tpy, confirms the formation of the complexes **[Cu1]** and **[Cu2]**, respectively. The presence of a metal-based peak in both Cu complexes was further confirmed by differential pulse voltammetry technique when scanned in a cathodic direction

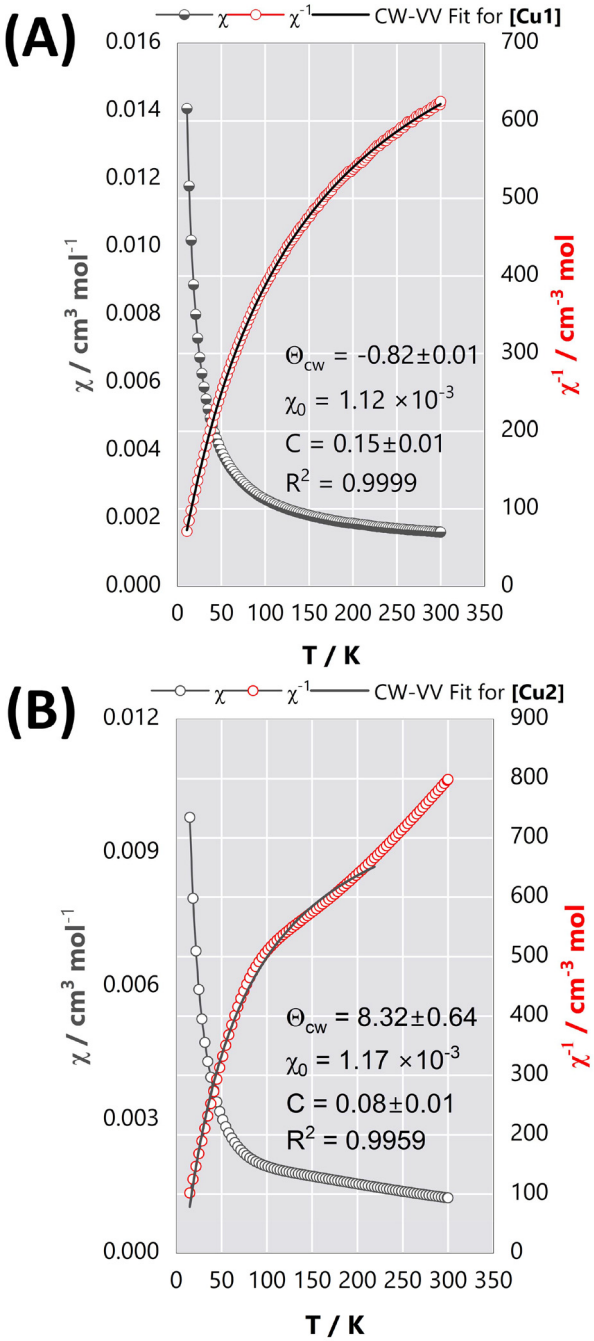

Fig. 2 Solid-state magnetic susceptibility of (A) **[Cu1]** and (B) **[Cu2]**, with corresponding fitting.

(Fig. 3a & b). Moreover, varying the scan rate in both complexes from 40–120 mV s^{-1} leads to a subsequent enhancement in the cathodic and anodic peak currents (Fig. S16). Furthermore, the two electrons had been involved due to Cu metal center was verified through coulometry at E_{app} = −0.60 V *vs.* SCE (Fig. S17 & S18). The resting potential of both **[Cu1]** and **[Cu2]** is approximately +0.1 V *vs.* SCE, suggesting that each complex undergoes a two-electron redox process involving the reduction of Cu^{2+} to Cu^0 and reoxidation back to Cu^{2+}. The

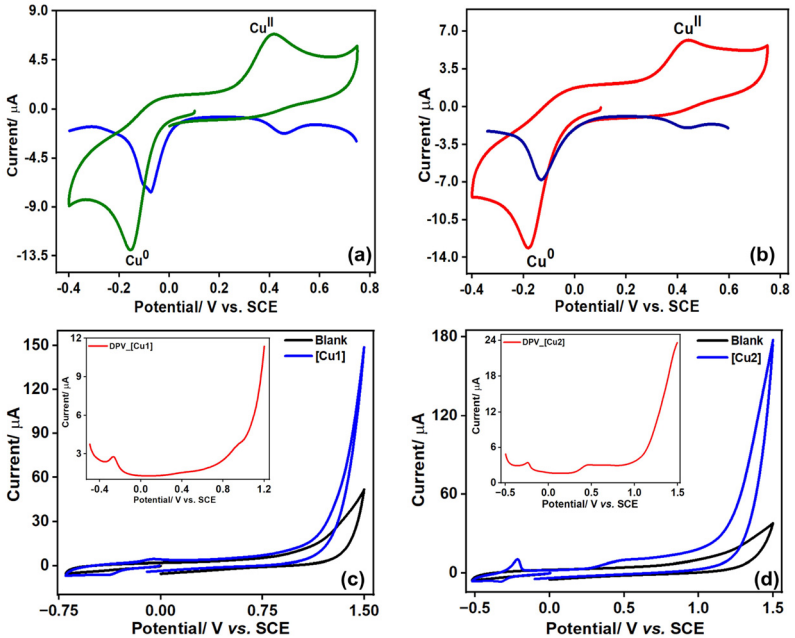

Fig. 3 Redox chemistry in DMF medium at a scan rate of 0.1 V s^{-1} using 0.1 M TBAP as a supporting electrolyte under an anaerobic atmosphere of 1.00 mM of complex (a) **[Cu1]** and (b) **[Cu2]**. Cyclic voltammogram in 0.1 M phosphate buffer at pH = 12.0 at a scan rate of 0.1 V s^{-1} under an inert atmosphere of 1.00 mM of catalyst (c) Full range CV of **[Cu1]**. Inset show the DPV of **[Cu1]** in 0.1 M phosphate buffer at pH = 12.0. (d) Full range CV of **[Cu2]**. Inset show the DPV of **[Cu2]** in 0.1 M phosphate buffer at pH = 12.0.

formation of Cu^{+} from Cu^{2+} during the cathodic scan appears to be kinetically slow, as evidenced by the large peak separation observed in the voltammograms—indicative of an irreversible or sluggish electron transfer process. This behavior is further supported by scan rate–dependent studies (Fig. S16). The transient nature of the Cu(I) intermediate may be attributed to its instability in solution, leading to rapid disproportionation *via* $2Cu^{+} \rightarrow Cu^{0} + Cu^{2+}$. An evaluation of the scan rate from 50–150 mV s^{-1} for $Cu^{II/I}$ had been recorded within the potential window of 0.7 V to −0.1 V *vs.* SCE for complexes **[Cu1]** and **[Cu2]** in DMF medium (Fig. S19a & Fig. S20a). The peak current for the cathodic and anodic waves exhibits linear dependency on the square root of the scan rate (Fig. S19b & Fig. S20b). On linear fitting of the graphical plot and using eqn (3), the diffusion coefficient value was found to be 0.0828 × 10^{-6} cm^2 s^{-1} and 0.0272 × 10^{-6} cm^2 s^{-1} for **[Cu1]** and 0.1107 × 10^{-6} cm^2 s^{-1} and 0.0377 × 10^{-6} cm^2 s^{-1} for **[Cu2]**, which infers that the process was diffusion-controlled under organic medium (Table S7 and S8).

$$i_P = 0.446\, nFA[\text{Catalyst}]\left(\frac{nFvD}{RT}\right)^{1/2} \quad (3)$$

Aqueous electrochemistry

The catalytic activity of both copper complexes as WOCs had been studied by cyclic voltammetry technique in 0.1 M phosphate buffer at pH = 12.0 by utilizing a glassy carbon as the working electrode under inert conditions. Upon performing both CV and DPV on 1.00 mM of complex **[Cu1]**, an irreversible peak attributed to the $Cu^{I/II}$ redox couple was noted at $E_{1/2}$ = −0.192 V *vs.* SCE ($E_{p,a}$ = −0.043 V & $E_{p,c}$ = −0.427 V *vs.* SCE). The complex exhibits another irreversible peak ascribed to ligand-based oxidation, which appears at $E_{p,a}$ = 0.989 V *vs.* SCE (Fig. 3c).

Under similar electrochemical conditions, the CV & DPV of 1.00 mM of complex **[Cu2]** exhibits an irreversible $Cu^{I/II}$ redox couple peak at E = −0.135 V *vs.* SCE ($E_{p,a}$ = −0.074 V & $E_{p,c}$ = −0.344 V *vs.* SCE). A broad irreversible peak corresponding to the $Cu^{II/III}$ redox couple had been observed at $E_{p,a}$ = 0.512 V *vs.* SCE (Fig. 3d). The diffusion coefficient for the electrocatalyst **[Cu1]** was assessed by the $Cu^{I/II}$ peak current with the scan rate dependence varying from 100–500 mV s^{-1} (Fig. S21a). The value was further estimated by the Randles–Sevcik eqn (3). The response of the peak current for the cathodic and anodic segment for **[Cu1]** suggests linear dependency with the square root of the scan rate, thereby illustrating diffusion-controlled phenomena (Fig. S21b). On linear fitting of the graphical plot and using eqn (2a) and (2b), the diffusion coefficient was found to be 1.056 × 10^{-6} cm^2 s^{-1} and 0.0192 × 10^{-6} cm^2 s^{-1} for the cathodic and anodic waves, respectively. Under similar electrochemical conditions (Fig. S22a), the complex **[Cu2]** exhibits linear dependency between the square root of the scan rate with the cathodic and anodic peak currents (Fig. S22b), and thereby possesses a diffusion coefficient value of 0.9704 × 10^{-6} cm^2 s^{-1} and 2.362 × 10^{-6} cm^2 s^{-1}, respectively[37] (Tables S9 and S10). Therefore, it can be inferred that both **[Cu1]** and **[Cu2]** can be utilized as active electrocatalysts for OER in 0.1 M phosphate buffer at pH = 12.0. Moreover, to assess the broader

applicability of the catalyst, its catalytic activity was examined from neutral to weakly alkaline medium (pH = 7.0 to 9.0) in 0.1 M phosphate buffer (Fig. S23).

Concentration variation of the catalyst

To gain insight into the kinetics of the OER, CV of both copper complexes was recorded by varying the catalyst concentration from 0.50 mM to 2.00 mM in 0.1 M phosphate buffer at pH = 12.0 (Fig. 4).

Moreover, a linear rise in the catalytic current (i_{cat}) with the enhancement of the catalyst concentration from 0.50 mM to 2.00 mM confirms the single-site molecular water oxidation, and is a characteristic feature of first-order WNA (Fig. S24 and S25) in the catalytic cycle.[40–42]

For a first-order oxygen evolution reaction where H_2O acts as both solvent and substrate, the calculated value of k_{cat} represents the limiting turnover frequency for the catalysts. It had been discerned that lowering the scan rate from 500 mV s^{-1} to 100 mV s^{-1} raises the ratio of i_{cat}/i_p, which was consistent with the rate-limiting O–O bond formation in the catalytic cycle (Fig. S26 and S27).[43–45]

Foot-of-the-wave analysis

Several transition metal complexes have been reported for the effective evolution of oxygen from water. Meanwhile, the contrasting experimental conditions under which catalysis occurs inhibit meaningful comparisons. However, as a consequence of several competing side reactions (such as substrate consumption, formation of metal oxides (MO_x), *etc.*), an ideal S-type catalytic current was not attained. In order to address such challenges, FOWA had been developed by Savéant *et al.*,[46] where kinetic information can be extracted even though an ideal S-type catalytic response is not obtained.[47a] A linear relationship between i_{cat}/i_p *vs.* the potential-dependent term had been noted for both WNA and I2M pathways (Fig. 5a). This potential-dependent term implies $[1/\{1 + \exp[(F/RT)(E - E_{cat/2})]\}]$ and $[1/\{1 + \exp[(F/RT)(E - E_{cat/2})]\}^{3/2}]$ for the WNA and I2M pathways, respectively, with each scientific term having significant meaning. The detailed calculations are provided in SI and (Tables S11–S14). The linear fitting between i_{cat}/i_p *vs.* the potential-dependent term yields a slope value through which the rate constant can be extracted (Fig. S30–S33). Furthermore, it had been discerned that the k_{WNA} value remains independent of the catalyst concentration (Fig. S34). The catalytic rate constant (k_D) assuming I2M pathway had also been evaluated. It was noted that the k_D value decreases with the increment in the catalyst concentration (Fig. S34). Hence, it can be inferred that the WNA mechanism was operative in both catalysts.[48] The TOF_{max} values calculated using foot-of-the-wave analysis of the reported Cu-based water oxidation catalysts are included in Table 1.

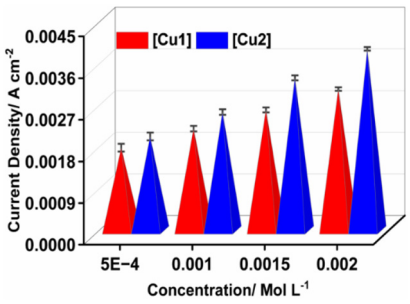

Fig. 4 Standard deviation plot of current density (at 1.5 V *vs.* SCE) *vs.* varying concentration of catalysts from 0.50 mM to 2.00 mM for **[Cu1]** and **[Cu2]** in 0.1 M phosphate buffer at pH = 12.0 under an anaerobic atmosphere.

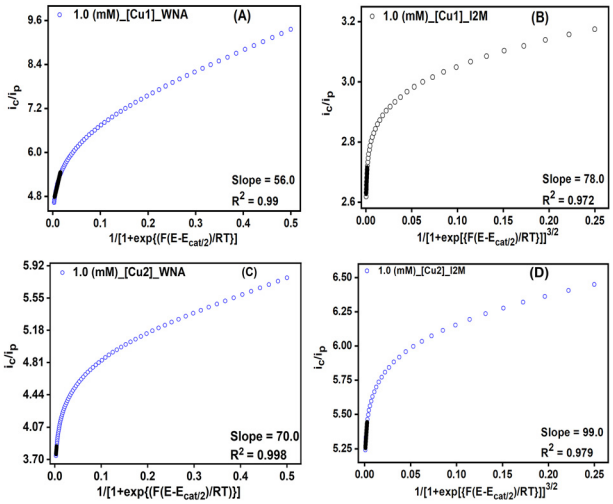

Fig. 5 FOWA plot in 0.1 M phosphate buffer at pH = 12.0, assuming the WNA pathway of (A) **[Cu1]** and (B) **[Cu2]**. FOWA plot in 0.1 M phosphate buffer at pH = 12.0, assuming the I2M pathway for (C) **[Cu1]** and (D) **[Cu2]**.

Catalytic Tafel plot

The catalytic Tafel plot provides valuable insights between the kinetic parameter (TOF) and thermodynamic overpotential (η). Under non-standard condition, the oxidation potential for oxygen liberation can be evaluated using the Nernst eqn (4), as follows:

$$E_{ox} = E^{\circ}_{ox} + \frac{0.059}{4}\log\frac{[H^+]^4}{[H_2O]} \text{ vs. NHE} \quad (4)$$

In general, the catalytic Tafel plot gives an idea about the change in TOF per unit change in η (Fig. S35–S38) for a particular catalyst, thereby indicating the reliance of TOF on the additional driving force beyond the thermodynamic requirement.[47b] In the catalysts **[Cu1]** and **[Cu2]**, the onset potential (E_{onset}) at varying concentrations from 0.50 mM–2.00 mM had been determined *vs.* SCE.

Moreover, the catalytic half-wave potential ($E_{cat/2}$) and TOF_{max} at each concentration had been evaluated (Tables S11–S14). These parameters were useful as they provide an in-depth understanding of the catalytic activity of each complex and their performance as electrocatalysts in OERs. A better catalyst was anticipated to exhibit a catalytic Tafel plot which gets

Table 1 Comparison of TOF_{max} calculated using foot-of-the-wave analysis for reported Cu-based water oxidation catalyst

Sl. no.	Catalyst	TOF_{max} (s^{-1})	Ref.
1	$[(PMOA)Cu]^{2-}$	3.56 (pH = 11.5) 12.0 (pH = 12.5)	25
2	$[Cu(dpaq)](ClO_4)$	3.1×10^2 (pH = 11.5)	45*e*
3	$[Cu(N_2O_2)]^{2-}$	54.0 (pH = 9.2)	45*b*
4	$[BPTCu^{II}(OH)_2]$	5.80 (pH = 11.5)	
5	$[Cu_2(BEE)_2]$ $[Cu_2(BE)_2]$	5503 (pH = 9.35) 51 (pH = 9.35)	49
6	$[(TAML)Cu](NMe_4)_2$	200 (pH = 12.0) 140 (pH = 7.0)	50
7	$[Cu(QCl\text{-}Tpy)Cl_2]$	10×10^3 (pH = 12.0)	This Work
8	$[Cu(8HQ\text{-}Tpy)Cl_2]$	15×10^3 (pH = 12.0)	This Work

PMOA = N_1,N'_1-(1,2-phenylene)bis(N_2-methyl-oxalamide); H-dpaq = 2-[bis(pyridin-2-methyl)amino-*N*-quinolin-8yl-acetamide]; N_2O_2 = *N*,*N*′-(1,2-phenylene)bis(2-hydroxy-2-methylpropanamide); BPT = peptoid trimer bearing a 2,2′-bipyridine ligand, a –OH group, and a benzyl group BEE = peptoid trimer having one 2,2′-bipyridine ligand, and two ethanolic groups; TAML = (15,15-dimethyl-8,13-dihydro-5*H*-dibenzo[*b*,*h*][1,4,7,10]tetraazacyclotridecine-6,7,14,16(15*H*,17*H*)-tetraone).

shifted diagonally to the upper left, signifying its superior performance and efficiency (Fig. S29).

Concentration variation of the phosphate buffer

Electrochemical measurements were conducted to examine the effect of the phosphate buffer on the oxygen evolution reaction by gradually increasing its concentration from 0.02 M to 0.10 M (Fig. S39 & S40) in the presence of 0.5 M $NaClO_4$. The linear rise in the current density at a fixed concentration of catalysts at 1.5 V *vs.* SCE with the increment of the phosphate buffer concentration indicates the strong ability of HPO_4^{2-} as a proton acceptor from nucleophilic H_2O to facilitate O–O bond formation.[51–53] The stability test for redox states was also performed using 0.1 M phosphate buffer at pH = 12.0 for both Cu complexes. The peak position for both catalysts remains constant after seven cycles, indicating the potential stability of the redox states under the experimental condition (Fig. S39f & S40f).

pH dependence electrochemical studies

The pH-dependent electrochemical studies were carried out by performing differential pulse voltammetry (Fig. S41) on 1.00 mM of both Cu complexes in Britton–Robinson buffer by varying the pH from 7.0–12.0 (Fig. 6). Initially, the catalyst **[Cu1]** exhibits a slope of 28 mV/pH, indicating a two electron-one proton transfer ($2e^-/1H^+$ PCET) occurring simultaneously to generate the $[Cu^{II}–OH]$ active species (L = QCl-Tpy).

$$[Cu^0(L)(Cl)(OH_2)]^{-1} \rightleftharpoons [Cu^{II}(L)(Cl)(OH)] + H^+ + 2e^-$$

The $[Cu^{II}–OH]$ active species undergoes oxidation to generate the $[Cu^{III}–OH]$ species, which followed by PCET generates the electron-deficient $[Cu^{II}–O^{\bullet}]$ species.

$$[Cu^{II}(L)(Cl)(OH)] \rightleftharpoons [Cu^{III}(L)(Cl)(OH)]^{+1} + e^-$$

$$[Cu^{III}(L)(Cl)(OH)]^{+1} \rightleftharpoons [Cu^{II}(O^{\bullet})(L^{\bullet+})(Cl)]^{+1} + H^+ + e^-$$

This species undergoes WNA on the oxygen center of the $[Cu^{II}–O^{\bullet}]$ species to form the hydro-peroxo species.

$$[Cu^{II}(L^{\bullet+})(Cl)(O^{\bullet})]^{+1} + OH^- \rightleftharpoons [Cu^{II}(L)(Cl)(–O–OH)]$$

The hydro-peroxo species releases one proton and one electron to form the superoxo species, which further undergoes nucleophilic attack by the OH^- ions present in the reaction medium to revert to the $[Cu^{II}–OH]$ active species with the liberation of an oxygen molecule.

$$[Cu^{II}(L)(Cl)(–O–OH)] \rightleftharpoons [Cu^{II}(L)(Cl)(–O–O^{\bullet})] + H^+ + e^-$$

$$[Cu^{II}(L)(Cl)(–O–O^{\bullet})] + OH^- \rightarrow [Cu^{II}(L)(Cl)(OH)] + e^- + O_2$$

On the other hand, the catalyst **[Cu2]** exists in a +2-oxidation state, which undergoes PCET ($1H^+/1e^-$) to form the $[Cu^{II}$-OH] species. This species further undergoes two proton and two electron transfer (PCET) simultaneously to form the $[Cu^{II}(–O^{\bullet})(L^{\bullet})(Cl)]$ species (where LH = 8HQ-Tpy).

$$[Cu^{I}(LH)(Cl)(OH_2)] \rightleftharpoons [Cu^{II}(OH)(LH)(Cl)] + H^+ + e^-$$

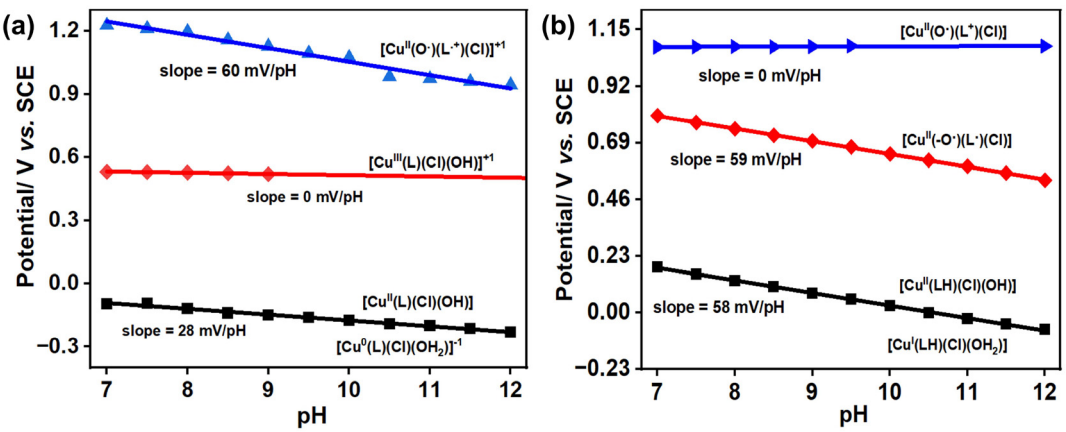

Fig. 6 Pourbaix diagram in Britton–Robinson buffer from pH = 7.0 to 12.0 of 1.00 mM of complexes (a) **[Cu1]** and (b) **[Cu2]**.

$$[Cu^{II}(LH)(Cl)(OH)] \rightleftharpoons [Cu^{II}(-O^{\bullet})(L^{\bullet})(Cl)] + 2H^{+} + 2e^{-}$$

The intermediate $[Cu^{II}(-O^{\bullet})(L^{\bullet})(Cl)]$ species further undergoes WNA by the HO^{-} ion with the release of one electron to form the Cu(II)-hydroperoxyl radical species.

$$[Cu^{II}(-O^{\bullet})(L^{\bullet})(Cl)] + OH^{-} \rightleftharpoons [Cu^{II}(-O^{\bullet}\text{–}OH)(L)(Cl)] + e^{-}$$

$$[Cu^{II}(-O^{\bullet}\text{–}OH)(L)(Cl)] \rightleftharpoons [Cu^{II}(-O\text{–}O^{\bullet})(L^{\bullet})(Cl)] + H^{+} + e^{-}$$

$$[Cu^{II}(O\text{–}O^{\bullet})(L^{\bullet})(Cl)] + OH^{-} + H^{+} \rightarrow [Cu^{II}(LH)(Cl)(OH)] + O_2$$

The hydroperoxyl radical species further undergoes one proton and one electron transfer and forms the Cu(II)-superoxo species, which upon nucleophilic attack by HO^{-} releases an O_2 molecule and reverts to its initial state.

Spectro-electro chemistry

The spectro-electrochemical properties of both catalysts **[Cu1]** and **[Cu2]** were studied through *in situ* FT-IR (Fig. 7 and S42) in 0.1 M phosphate buffer at pH = 12.0. The transient copper super-oxo species had been detected through CPE at 1.35 V *vs.* SCE (Fig. 7). Initially, the IR spectra of the complex show no peaks at around 1110–1120 cm^{-1}, indicating that the catalyst exists in the $[Cu^{II}\text{–}OH]$ state. Through the CPE technique, it was observed that the band intensity at 1110–1120 cm^{-1} was enhanced with increasing electrolysis time. The band noted at 1110–1120 cm^{-1} was mainly attributed to the formation of the transient cupric super-oxo transient species ($\nu_{O\text{–}O}$ = 1112 cm^{-1}).[54a–c] This similarity in stretching frequencies lends more credence to the idea that the super-oxo ion coordinates with the copper metal center in both catalysts during oxidation of H_2O. Similarly, the addition of a certain aliquot of H_2O_2 leads to the generation of a discernible IR peak at 800–900 cm^{-1} (Fig. S42), corresponding to the end-on stretching frequency of the transient cupric-hydroperoxo $[Cu^{II}\text{–}OOH]$ species.[54d] The peak intensity is enhanced with the increment in the amount of added H_2O_2.

Homogeneity study

To investigate whether the catalytic process in both copper complexes was homogeneous, several controlled potential experiments were performed, which indicated that the catalysts retained their molecular nature without being deposited on the electrode surface. Initially, minimal changes in the absorption spectra (Fig. S43) and cyclic voltammogram of both complexes (Fig. S44) were noted when recorded in 0.1 M phosphate buffer at pH = 12.0 before and after applying the potential of 1.5 V *vs.* SCE for 2 hours, indicating no change in the structural integrity.[55] Moreover, the mass spectrometry data of both complexes after CPE at 1.5 V *vs.* SCE for 2 hours (Fig. S45 & S46) illustrate the minute shift in the peak, thereby suggesting that **[Cu1]** and **[Cu2]** were still the major species existing in the solution.[56]

As a support to our analysis, a rinse test (charge built-up test) was performed for both complexes, where the GC electrode had been subjected to CPE at 1.5 V *vs.* SCE in the presence of the complexes for 2 hours in 0.1 M phosphate buffer at pH = 12.0, and the amount of accumulated charge was observed. The same GC electrode was reused by rinsing with water and dipped in fresh 0.1 M phosphate buffer solution having pH = 12.0 in the absence of complexes, and was allowed to undergo electrolysis at 1.5 V *vs* SCE for 2 hours. The amount of charge accumulated after the rinse test was less in **[Cu1]** (Fig. S47a), whereas the charge accumulated in **[Cu2]** was identical to that of the blank (Fig. S47b), thereby excluding the deposition of any CuO_x particles on the electrode surface.[49,57] Furthermore, examination of the GC electrode in the presence and absence of the catalyst by FESEM (Fig. S48 and S49), EDX (Fig. S50 and S51), XPS (Fig. S52a and S52b), and DLS measurement (Fig. S52c & S52d) upon CPE at 1.5 V *vs.* SCE for 2 hours concludes that nanoparticles $(CuO)_x$ were not formed during electrolysis.[58–60]

Electron paramagnetic resonance

From the EPR spectra of complexes **[Cu1]** and **[Cu2]** in MeOH solvent at 77 K (Fig. S53), it had been noted that the geometry of both catalysts remains square pyramidal with unpaired elec-

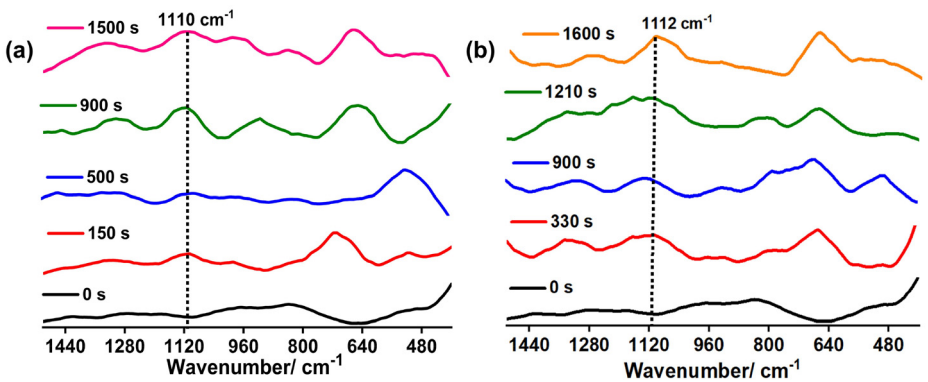

Fig. 7 Detection of the super-oxo transient intermediate species in 0.1 M phosphate buffer at pH = 12.0 through CPE at 1.35 V *vs.* SCE by *in situ* FT-IR spectroscopy technique using 1.25 mM of complexes (a) **[Cu1]** and (b) **[Cu2]**.

trons residing in the d_{x^2}– d_{y^2} orbital,[61] which had been consistent with the *g*-tensor values of $g_x = g_y = g_\perp = 2.08$ and $g_z = g_\parallel = 2.15$ for **[Cu1]** and of $g_x = g_y = g_\perp = 2.045$ and $g_z = g_\parallel = 2.28$ for **[Cu2]**. All the simulated parameters are listed in Table 2 and Tables S15 and 16.

The EPR spectra of **[Cu1]** and **[Cu2]** before and after electrolysis at 77 K in 0.1 M phosphate buffer (pH = 12.0) are presented in Fig. 8(a)–(d). The simulated parameters are tabulated in Table 2. Upon simulation, it had been noted that catalysts **[Cu1]** and **[Cu2]** possess *g*-tensor values of $g_z = g_\parallel = 2.23$ and 2.32, respectively. Furthermore, a prominent signal at $g_x = g_y = g_\perp = 2.05$ and 2.08 for **[Cu1]** and **[Cu2]**, respectively, demonstrate a typical derivative line shape. The observed trend in g-values ($g_\parallel > g_\perp > 2.0023$) for both Cu complexes indicates that an unpaired electron occupies the $d_{x^2} - d_{y^2}$ orbital of the pentacoordinated square pyramidal geometry.[37c,61a,b] This observation was consistent with a Cl-donor ligand (weaker ligand), revealing a bond in the axial plane of the square pyramidal geometry.

An EPR spectrum recorded at 77 K after performing CPE in 0.1 M phosphate buffer at pH = 12.0, as shown in Fig. 8(b), suggests a structural change with the *g*-tensor values of $g_z = 2.22$, $g_y = 2.105$ and $g_x = 2.03$, which might be possible due to the formation of a phosphate-coordinated copper(II) species in the primary coordination sphere of the complex. The linear combination of the $d_{x^2} - d_{y^2}$ and d_{z^2} ground states cause this feature, which was usually an intermediate between the trigonal bipyramidal and square pyramidal geometries, as evidenced by eqn (5)–(7):[61c]

$$\Psi_{gs} = c_1|d_{z^2}\rangle + c_2|d_{x^2} - d_{y^2}\rangle \quad (5)$$

where c_i represents the coefficients of the linear combinations.

For complexes of such type, a parameter *R* can be indicative of the predominance of the d_{z^2} ($c_1 > c_2$) or $d_{x^2} - d_{y^2}$ orbital ($c_2 > c_1$) in the ground state,[61b] as represented in eqn (6):

$$g_\perp = g_x = g_y = 2.0023 \pm \frac{6\lambda}{E(d_{z^2}) - E(d_{xz})} = 2.0023 \pm \frac{6\lambda}{E(d_{z^2}) - E(d_{yz})} \quad (6)$$

$$R = \frac{g_y - g_z}{g_x - g_y} \quad (7)$$

where *R* can be indicative of the predominance of the $d_{x^2} - d_{y^2}$ and d_{z^2} ground states. From eqn (7), it had been noted that $R > 1$, which implies that the ground state arises from the d_{z^2} orbital. Upon performing CPE under similar electrochemical conditions for **[Cu2]**, similar EPR spectra (Fig. 8d) had been observed as that for the condition before CPE (Fig. 8c) with *g*-tensor values being $g_x = g_y = g_\perp = 2.065$ and $g_z = g_\parallel = 2.18$.

Table 2 Simulated parameters for the EPR spectra

	g-Matrix			*A*-Matrix/G			*D* Matrix/G	
Fig. no.	g_x	g_y	g_z	A_x	A_y	A_z	*D*	*E*
8(a)	2.05	2.05	2.23	—	150	—	—	—
8(b)	2.03	2.105	2.22	—	—	100	—	—
8(c)	2.08	2.08	2.32	60	20	160	1	0.33
8(d)	2.07	2.07	2.18	—	—	60	—	—

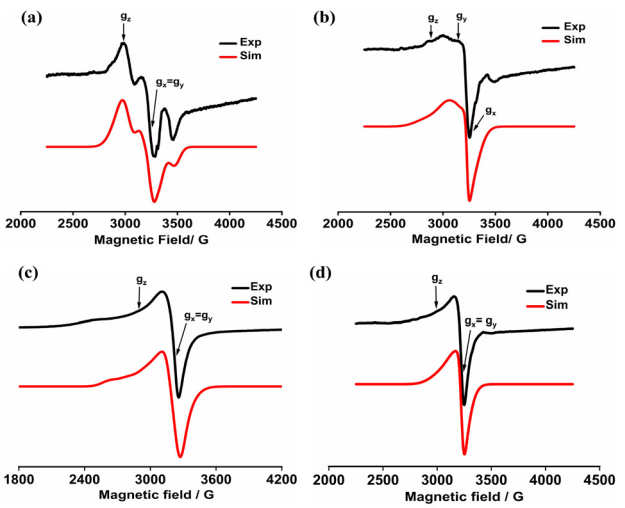

Fig. 8 X-band EPR spectra recorded at 77 K in 0.1 M phosphate buffer at pH = 12.0 for 1.50 mM of: (a) **[Cu1]** before electrolysis, (b) **[Cu1]** after electrolysis, (c) **[Cu2]** before electrolysis, and (d) **[Cu2]** after electrolysis.

Controlled potential electrolysis

The liberation of O_2 by both complexes had been quantified by conducting CPE in 0.1 M phosphate buffer at pH = 12.0 at an applied potential of 1.35 V *vs.* SCE for 350 seconds.[23a] The amount of charge accumulated due to complexes **[Cu1]** and **[Cu2]** was observed to be high in comparison to the total charge passed in their absence. The evolved O_2 had been detected and quantified by utilizing an optical fibre oxygen sensor. The result illustrates a steady rise in O_2 evolution by both copper complexes (Fig. 9). The low faradaic efficiency (F.E.) of the complexes (F.E. = 68.0% for **[Cu1]**; F.E. = 83.0% for **[Cu2]**) might be attributed to the oxidative degradation of carbon electrodes.[50] Moreover, the headspace had not been able to detect any residual O_2 remaining dissolved in solution. To access the broader applicability of the complexes, its catalytic activity was examined from neutral to weakly alkaline media (pH = 7.0 to 9.0) in 0.1 M phosphate buffer (Fig. S54).

DFT characterization of water oxidation

Density functional theory (DFT)[62,63] calculations were performed using the Gaussian 16 package[64] to explore the mechanistic insight of the Cu catalyst oxygen evolution reaction (OER). For the geometry optimization and frequency calculation, the B3LYP function[65,66] was used with the Lanl2dz basis set[67] for the metal Cu center and 6-31+G* basis set[68] for other nonmetal centers (H, C, N, O, Cl). The computational details are given in SI. To decide the most stable spin state, we optimized all possible spin states of each molecule (Table S17). In the DFT free energy calculations, the chemical

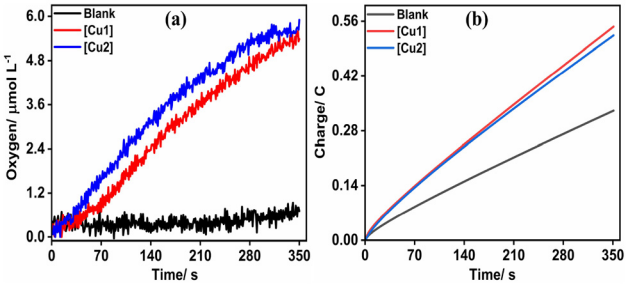

Fig. 9 (a) Direct O_2 measurement of complexes **[Cu1]** and **[Cu2]**. (b) Total charge build-up during controlled potential electrolysis. Electrolysis conditions: 0.50 mM of the catalyst in 0.1 M phosphate buffer at pH = 12.0 using three-electrode configurations under an inert atmosphere.

potential H^+/e^- pairs were taken as one-half of the H_2 potential, considering the computational hydrogen electrode model.[69] To avoid errors associated with the Gibbs free energy of O_2, we used the free energies of H_2O and H_2, including the 4.93 eV experimental correction value. The calculated oxidation potentials are provided in Tables S18 and S19. The potential limiting step (PLS) was identified as the most thermodynamically demanding step.

$$\mu_{O_2} = 2G_{H_2O} - 2G_{H_2} + 4.93 \text{ eV} \quad (8)$$

In the oxygen evolution reaction (OER) pathway, the OH group coordinates with metal catalysts in alkaline medium (pH = 12) and undergoes proton-coupled electron transfer (PCET) processes to generate a metal oxyl species.[70] Furthermore, metal oxyl species participate in nucleophilic reactions with hydroxide molecules, creating peroxide and superoxide intermediates *via* consecutive proton–electron transfer reactions (Fig. 10). Here, OER is investigated in the presence of two Cu-based catalysts that contain Cl (**a**) and OH (**b**) functional groups.

Catalyst **Int-1a** is penta-coordinated with three sp^2 hybridized N centers, one Cl and one OH, and the doublet state was the most stable electronic state. In the first step of the reaction, **Int-1a** was oxidized to **Int-2a**, followed by the PCET reaction. After the oxidation of **Int-1a**, the Cu–OH bond distance was increased from 1.87 to 2.15 Å. The calculated potential for the oxidation of **Int-1a** to **Int-2a** is −0.60 V (*vs.* SCE). The calculated reaction energy for the oxidation reaction is 1.55 eV. In the first PCET reaction, the formation of **Int-3a** from **Int-2a** took place with a 1.31 eV free energy change. The oxyl intermediate **Int-3a** further undergoes an OH addition reaction to generate the hydroperoxide intermediate **Int-4a** (Fig. 10). The **Int-4a** formation can proceed through the **TS-1a** with a [Cu–O] bond distance of 1.88 Å, whereas the O–OH (hydroperoxo) bond distance is 2.37 Å with a free energy barrier of 1.09 eV (Fig. 11). The HOMO–LUMO distribution (Fig. S56) suggests that the HOMO of **Int-3a** was primarily present at the ligand center, and the LUMO was distributed around the Cu–O bonds. During the reaction, hydroxide undergoes an addition reaction with the metal oxyl complex **Int-3a** *via* single electron transfer reaction (SET), where the LUMO of **Int-3a** interacts with the HOMO of the OH group. The reaction was exothermic with −2.48 eV reaction energy. **Int-4a** proceeds further for a PCET reaction with 0.76 eV reaction energy in the next step. The potential limiting step was identified as the most thermodynamic energy-demanding step among all steps, and it is the first reduction reaction (**Int-1a** to **Int-2a**) with 1.55 eV energy.

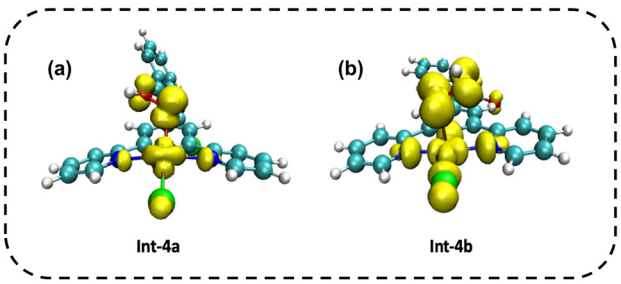

Fig. 10 Spin density distribution of (a) **Int-4a** and (b) **Int-4b**.

Considering the reaction by catalyst **b** in Fig. 12, two PCET transfer reactions of **Int-1b** may either proceed through step-by-step PCET reactions or simultaneous two PCET reactions at pH = 12 to generate **Int-3b**. In the stepwise reaction, the ligand OH dissociation reaction had lower energy demand than the metal-coordinated OH group, with respective reaction energies of 0.44 and 1.63 eV. The spin density distribution indicates (Fig. S57, Table S20) that after the ligand OH dissociation, the spin density was distributed adjacent to the aromatic ring, which may accelerate the ligand OH dissociation. The metal oxyl complex **Int-3b** reacts with hydroxide followed by reduction to generate **Int-4b** with an energy barrier of 1.26 eV and a reaction energy of −2.28 eV (Fig. 12). Next, the metal hydroperoxide radical species **Int-4b** was converted into **Int-5b** *via* a PCET reaction with a reaction energy of −0.47 eV. The DFT calculation suggests that the formation of **Int-3b** *via* the second PCET reaction was the potential limiting step with 1.63 eV energy. The intermediates **Int-5a** and **Int-5b** on nucleophilic attack by OH^-, releases O_2 and reverts to the **Int-1a** and **Int-1b**, respectively.

Therefore, in the presence of catalyst **b**, the OH bond dissociation reaction in the second PCET reaction is the potential limiting step. The mechanistic study also suggests that the ligand-carrying OH group in catalyst **b** is redox non-innocent and plays an important role by directly participating in the reaction. The calculated energy barrier for some of the reported Cu-based WOCs is provided in Table S21. The DFT calculated results indicate that the activation barrier for the specific peroxide formation step by catalyst **a** is lower than that of catalyst **b**. However, the transition state **TS-1a** in the energy profile diagram exists relatively higher than **TS-1b**. Here, both thermodynamic reaction energy and kinetic barrier significantly control the overall catalytic performance of the reaction. The lower energy span associated with the **TS-1b** transition state compared to **TS-1a** enhances the catalytic activity of catalyst **b**. This computational finding aligns well with our experimental observations.

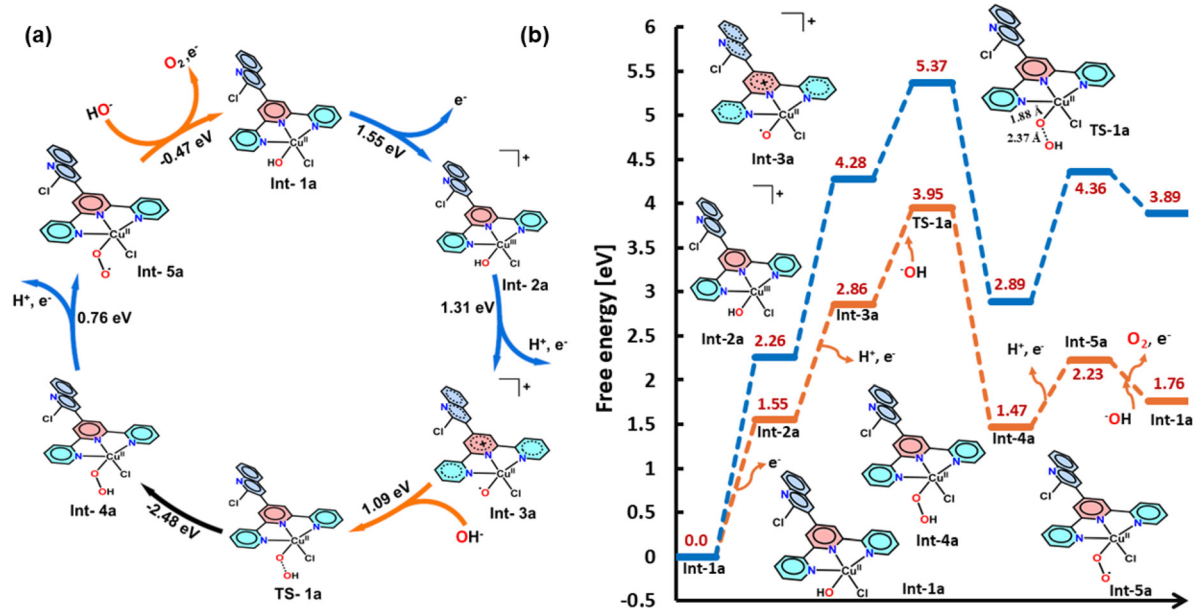

Fig. 11 (a) Catalytic cycle for the complete oxygen evolution reaction by catalyst **a**. (b) Energy profile diagram for catalyst **a**, where the blue path is shown without the pH correction factor and the orange path is shown with the pH correction factor at pH = 12 (all values are in eV).

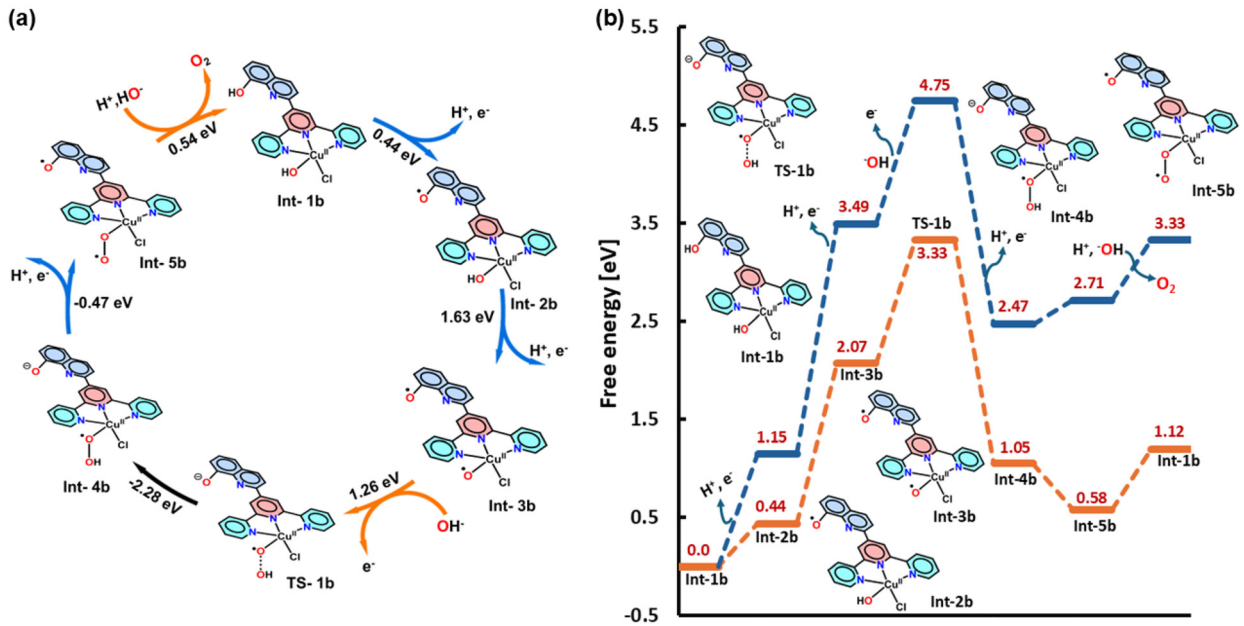

Fig. 12 (a) Catalytic cycle for the complete oxygen evolution reaction by catalyst **b**. (b) Energy profile diagram for catalyst **b**, where the blue path is shown without the pH correction factor and the orange path is shown with the pH correction factor at pH = 12 (all values are in eV).

Conclusions

In summary, we have reported two highly active and robust Cu complexes, **[Cu1]** and **[Cu2]**, supported on a redox-active substituted terpyridine ligand framework, which efficiently oxidizes H_2O to O_2. The complexes **[Cu1]** and **[Cu2]** exhibit an impressive TOF_{max} value (from FOWA) of 10×10^3 s^{-1} and 15×10^3 s^{-1}, respectively. Both catalysts evolve oxygen under a highly alkaline medium in 0.1 M phosphate buffer at pH = 12.0 with an overpotential of 780 mV for catalyst **[Cu2]** and 830 mV for **[Cu1]**. Experimental observation in FOWA indicates that **[Cu2]** is a slightly better catalyst for the reaction. The kinetic studies, catalytic Tafel plot, and faradaic efficiency infer that complex **[Cu2]** acts as a slightly better catalyst in comparison to **[Cu1]**. Besides experimental studies, DFT calculations affirm that both catalysts follow first-order kinetics, and therefore undergo water nucleophilic attack to liberate O_2.

Author contributions

D. R. curated the data, performed the formal analysis of the data and wrote the original draft of the manuscript. K. M. conducted the DFT calculations, performed the formal DFT analysis and wrote the original draft of the manuscript. M. R. conducted the experiments. A. M. collected the EPR data. R. M. curated the data. T. P. curated the data. B. S. M. verified the DFT calculations and provided the source for the computational studies. S. K. P. conceived the idea, provided the resources, supervised the work and modified the original manuscript draft.

Conflicts of interest

The authors declare that there are no conflicts of interest.

Data availability

Supplementary information: details of materials and instrumentation, characterization of ligands and complexes, X-ray structure analysis, bond lengths, bond angles, magnetic measurement details, electrochemistry experiments, bulk electrolysis, gas evolution and cartesian coordinates. See DOI: **https://doi.org/10.1039/d5dt01397f**.

CCDC 2400502 and 2400503 contain the supplementary crystallographic data for this paper.[71a,b]

Acknowledgements

This work was executed at the Indian Institute of Technology (Indian School of Mines) Dhanbad's Artificial Photosynthesis Laboratory, Department of Chemistry and Chemical Biology. S. K. P. is grateful for the CSIR grant 01(3062)/21/EMR-II. The SC-XRD, HRMS, FESEM, EDX, and XPS facilities provided by CRF IIT (ISM) Dhanbad are acknowledged by the authors. The authors thank the Department of Chemistry, IISER Kolkata and Shiv Nadar University for providing the EPR facilities. The authors additionally thank IIT Kharagpur for the temperature-dependent magnetic susceptibility data from the Quantum Design MPMS SQUID VSM Ever Cool system. The authors are grateful to Prof. Yulia Pushkar from Purdue University for fruitful discussions and suggestions. The authors are grateful to Prof. Sagar Pal from IIT(ISM) Dhanbad for providing facilities for the DLS study. The authors gratefully acknowledge Prof. Ebbe Nordlander (Lund University, Sweden) for his valuable discussions and suggestions.

References

1 M. D. Kärkäs and B. Åkermark, *Dalton Trans.*, 2016, **45**(37), 14421–11446.
2 B. Zhang and L. Sun, *Chem. Soc. Rev.*, 2019, **48**(7), 2216–2264.
3 J. D. Blakemore, R. H. Crabtree and G. W. Brudvig, *Chem. Rev.*, 2015, **115**(23), 12974–13005.
4 (*a*) M. Yu, E. Budiyanto and H. Tüysüz, *Angew. Chem., Int. Ed.*, 2022, **61**(1), e202103824; (*b*) B. M. Hunter, H. B. Gray and A. M. Müller, *Chem. Rev.*, 2016, **116**(22), 14120–14136.
5 T. J. Meyer, M. V. Sheridan and B. D. Sherman, *Chem. Soc. Rev.*, 2017, **46**(20), 6148–6169.
6 S. Fukuzumi, Y.-M. Lee and W. Nam, *Dalton Trans.*, 2019, **48**(3), 779–798.
7 N. Cox, M. Retegan, F. Neese, D. A. Pantazis, A. Boussac and W. Lubitz, *Science*, 2014, **345**(6198), 804–808.
8 F. Umena, K. Kawakami, J.-R. Shen and N. Kamiya, *Nature*, 2011, **473**(7345), 55–60.
9 J. S. Pap, Ł. Szyrwiel, D. Srankó, Z. Kerner, B. Setner, Z. Szewczuk and W. Malinka, *Chem. Commun.*, 2015, **51**(29), 6322–6324.
10 T. A. Betley, Q. Wu, T. V. Voorhis and D. G. Nocera, *Inorg. Chem.*, 2008, **47**(6), 1849–1861.
11 J. A. Halfen, S. Mahapatra, E. C. Wilkinson, S. Kaderli, V. G. Young, L. Que, A. D. Zuberbühler and W. B. Tolman, *Science*, 1996, **271**(5254), 1397–1400.
12 (*a*) A. Vatsa and S. K. Padhi, *Eur. J. Inorg. Chem.*, 2021, **2021**(34), 3499–3505; (*b*) L. Li, B. Das, A. Rahaman, A. Shatskiy, F. Ye, P. Cheng, C. Yuan, Z. Yang, O. Verho, M. D. Kärkäs, J. Dutta, T.-C. Weng and B. Åkermark, *Dalton Trans.*, 2022, **51**(20), 7957–7965; (*c*) A. K. Ravari, G. Zhu, R. Ezhov, Y. P. Galvan, A. Page, W. Weinschenk, L. Yan and Y. Pushkar, *J. Am. Chem. Soc.*, 2020, **142**(2), 884–893; (*d*) M. A. Hoque, A. D. Chowdhury, S. Maji, J. B. Buchholz, M. Z. Ertem, C. G. Suriñach, G. K. Lahiri and A. Llobet, *Inorg. Chem.*, 2021, **60**(2), 5791–5803; (*e*) B. J. J. Timmer, O. Kravchenko, B. Zhang, T. Liu and L. Sun, *Inorg. Chem.*, 2021, **60**(2), 1202–1207; (*f*) A. Singh, B. Singh, S. Dey, A. Indra and G. K. Lahiri, *Inorg. Chem.*, 2023, **62**(6), 2769–2783; (*g*) A. Kundu, S. K. Barman and S. Mandal, *Inorg. Chem.*, 2022, **61**(3), 1426–1437; (*h*) J. Shi, Y.-H. Guo, F. Xie, Q.-F. Chen and M.-T. Zhang, *Angew. Chem., Int. Ed.*, 2020, **59**(10), 4000–4008.
13 (*a*) J. F. Hull, D. Balcells, J. D. Blakemore, C. D. Incarvito, O. Eisenstein, G. W. Brudvig and R. H. Crabtree, *J. Am. Chem. Soc.*, 2009, **131**(25), 8730–8731; (*b*) B. V. Dijk, G. M. Rodriguez, L. Wu, J. P. Hofmann, A. Macchioni and D. G. H. Hetterscheid, *ACS Catal.*, 2020, **10**(7), 4398–4410.
14 M. A. Luna, F. Moyano, L. Sereno and F. D.′. Eramo, *Electrochim. Acta*, 2014, **135**, 301–310.
15 L. D. Wickramasinghe, R. Zhou, R. Zong, P. Vo, K. J. Gagnon and R. P. Thummel, *J. Am. Chem. Soc.*, 2015, **137**(41), 13260–13263.
16 D. D. Boer, Q. Siberie, M. A. Siegler, T. H. Ferber, D. C. Moritz, J. P. Hofmann and D. G. H. Hetterscheid, *ACS Catal.*, 2022, **12**(8), 4597–4607.
17 X. Chen, X. Liao, C. Dai, L. Zhu, L. Hong, X. Yang, Z. Ruan, X. Liang and J. Lin, *Dalton Trans.*, 2022, **51**(48), 18678–18684.
18 J. Lin, X. Chen, N. Wang, S. Liu, Z. Ruan and Y. Chen, *Catal. Sci. Technol.*, 2021, **11**(19), 6470–6476.

19 (*a*) R. Matheu, P. G. Barros, M. G. Sepulcre, M. Z. Ertem, X. Sala, C. G. Suriñach and A. Llobet, *Nat. Rev. Chem.*, 2019, **3**, 331–341; (*b*) J. W. Wang, D.-C. Zhong and T.-B. Lu, *Coord. Chem. Rev.*, 2018, **377**, 225–236.
20 C. E. Elwell, N. L. Gagnon, B. D. Neisen, D. Dhar, A. D. Spaeth, G. M. Yee and W. B. Tolman, *Chem. Rev.*, 2017, **117**(3), 2059–2107.
21 S. M. Barnett, K. L. Goldberg and J. M. Mayer, *Nat. Chem.*, 2012, **4**, 498–502.
22 (*a*) H. H. Huang, J.-W. Wang, P. Sahoo, D. C. Zhong and T. B. Lu, *Chem. Commun.*, 2017, **53**, 9324–9327; (*b*) C. Lu, J. Wang and Z. Chen, *ChemCatChem*, 2016, **8**(67), 2165–2170.
23 (*a*) K. J. Fisher, K. L. Materna, B. Q. Mercado, R. H. Crabtree and G. W. Brudvig, *ACS Catal.*, 2017, **7**(5), 3384–3387; (*b*) R.-J. Xiang, H.-Y. Wang, Z.-J. Xin, C.-B. Li, Y.-X. Lu, X.-W. Gao, H.-M. Sun and R. Cao, *Chem. – Eur. J.*, 2016, **22**(5), 1602–1607.
24 T. Zhang, C. Wang, S. Liu, J.-L. Wang and W. Lin, *J. Am. Chem. Soc.*, 2014, **136**(1), 273–281.
25 P.-G. Barros, I. F. Ardoiz, S. Drouet, J. B. Buchholz, F. Maseras and A. Llobet, *J. Am. Chem. Soc.*, 2015, **137**(21), 6758–6761.
26 L. A. Stott, K. E. Prosser, E. K. Berdichevsky, C. J. Walsby and J. J. Warren, *Chem. Commun.*, 2017, **53**(3), 651–654.
27 Y. Liu, Y. Han, Z. Zhang, W. Zhang, W. Lai, Y. Wang and R. Cao, *Chem. Sci.*, 2019, **10**(9), 2613–2622.
28 J. Shen, M. Wang, P. Zhang, J. Jiang and L. Sun, *Chem. Commun.*, 2017, **53**(31), 4374–4377.
29 Z. Xu, Z. Zheng, Q. Chen, J. Wang, K. Yu, X. Xia, J. Shen and Q. Zhang, *Dalton Trans.*, 2021, **50**(31), 10888–10895.
30 H. Kuliya, N. Alam, D. Sarma, D. Choudhury and A. Kalita, *Chem. Commun.*, 2019, **55**(38), 5483–5486.
31 J. Patel, K. Majee, E. Ahmad, A. Vatsa, B. Das and S. K. Padhi, *ChemistrySelect*, 2017, **2**(1), 123–129.
32 M. Raj and S. K. Padhi, *J. Heterocycl. Chem.*, 2019, **56**(3), 988–997.
33 (*a*) S. Khan, S. Sengupta, M. A. Khan, M. P. Sk, N. C. Jana and S. Naskar, *Inorg. Chem.*, 2024, **63**(4), 1888–1897; (*b*) S. Roy, S. Javed, M. M. Olmstead and A. K. Patra, *Dalton Trans.*, 2011, **40**(48), 12866–12876.
34 D. F. Evans, *J. Chem. Soc.*, 1959, 2003–2005.
35 D. K. Buysser, G. G. Herman, E. Bruneel, S. Hoste and V. I. Driessche, *Chem. Phys.*, 2005, **315**(3), 286–292.
36 (*a*) S. Mugiraneza and A. M. Hallas, *Commun. Phys.*, 2022, **5**, 95; (*b*) N. F. Chilton, R. P. Anderson, L. D. Turner, A. Soncini and K. S. Murray, *J. Comput. Chem.*, 2013, **34**(13), 1164–1175, DOI: **10.1002/jcc.23234**; (*c*) M. K. Paira, T. K. Mondal, E. L. Torres, J. Ribas and C. Sinha, *Polyhedron*, 2010, **29**(17), 3147–3156; (*d*) M. Malik, A. Świtlicka, A. Bieńko, U. K. Komarnicka, D. C. Bieńko, S. Kyzioł, A. Kyzioł, T. Mazur and B. Machura, *RSC Adv.*, 2022, **12**(42), 27648–27665; (*e*) N. Podjed, B. Modec, R. Clérac, M. Rouzières, M. M. Alcaide and J. L. Serano, *New J. Chem.*, 2022, **46**(15), 6899–6920; (*f*) M. Raj, K. Makhal, D. Raj, A. Mishra, B. S. Mallik and S. K. Padhi, *Dalton Trans.*, 2023, **52**(47), 17797–17809; (*g*) S. S. Akhter, D. Srivastava, A. Mishra, N. Patra, P. Kumar and S. K. Padhi, *Chem. – Eur. J.*, 2024, **30**(70), e202403321, DOI: **10.1002/chem.202403321**.
37 (*a*) A. Ali, D. Prakash, P. Majumdar, S. Ghosh and A. Dutta, *ACS Catal.*, 2021, **11**(10), 5934–5941; (*b*) K. Majee, J. Patel, B. Das and S. K. Padhi, *Dalton Trans.*, 2017, **46**(43), 14869–14879; (*c*) A. Mishra, D. Srivastava, D. Raj, N. Patra and S. K. Padhi, *Dalton Trans.*, 2024, **53**(3), 1209–1220; (*d*) P. Zhang, M. Wang, Y. Yang, T. Yao and L. Sun, *Angew. Chem., Int. Ed.*, 2014, **53**(50), 13803–13807.
38 E. Ahmad, S. Rai and S. K. Padhi, *Int. J. Hydrogen Energy*, 2019, **44**(33), 16467–16477.
39 M. Raj and S. K. Padhi, *Eur. J. Inorg. Chem.*, 2022, **2022**(21), e202200238.
40 D. L. Gerlach, S. Bhagan, A. A. Cruce, D. B. Burks, I. Nieto, H. T. Troung, S. P. Kelley, C. J. H. Gervasoni, K. L. Jernigan, M. K. Bowman, S. Pan, M. Zeller and E. T. Papish, *Inorg. Chem.*, 2014, **53**(24), 12689–12698.
41 M. K. Coggins, M.-T. Zhang, A. K. Vannucci, C. J. Dares and T. J. Meyer, *J. Am. Chem. Soc.*, 2014, **136**(15), 5531–5534.
42 L. Wang, L. Duan, R. B. Ambre, Q. Daniel, H. Chen, J. Sun, B. Das, A. Thapper, J. Uhlig, P. Dinér and L. A. Sun, *J. Catal.*, 2016, **335**, 72–78.
43 R. S. Nicholson and I. Shain, *Anal. Chem.*, 1964, **36**, 706–723, DOI: **10.1021/ac60210a007**.
44 M. T. Zhang, Z. Chen, P. Kang and T. J. Meyer, *J. Am. Chem. Soc.*, 2013, **135**(6), 2048–2051.
45 (*a*) T. Ghosh, P. Ghosh and G. Maayan, *ACS Catal.*, 2018, **8**, 10631–10640; (*b*) M. Bera, K. Keshari, A. Bhardwaj, G. Gupta, B. Mondal and S. Paria, *Inorg. Chem.*, 2022, **61**(7), 3152–3165; (*c*) T. Fang, L.-Z. Fu, L.-L. Zhou and S.-Z. Zhan, *Electrochim. Acta*, 2015, **161**, 388–394; (*d*) M. G. -Sepulcre, P. G. -Barros, J. Oldengott, I. F. -Ardioz, R. Bofill, X. Sala, J. B. Buchholz and A. Llobet, *Angew. Chem., Int. Ed.*, 2021, **60**(34), 18639–18644; (*e*) S. Biswas, S. N. Chowdhury, S. Das, S. Bose, J. Debgupta, S. Paul and A. N. Biswas, *ChemCatChem*, 2025, **17**(4), e202401357; (*f*) Q.-F. Chen, Z.-Y. Cheng, R.-Z. Liao and M.-T. Zhang, *J. Am. Chem. Soc.*, 2021, **143**(47), 19761–19768; (*g*) X. Zhang, Y.-Y. Li, J. Jiang, R. Zhang, R. Z. -Liao and M. Wang, *Inorg. Chem.*, 2020, **59**(8), 5424–5432; (*h*) Q.-Y. Mao, Y.-J. Pang, X.-C. Li, G.-J. Chen and H.-W. Tan, *ACS Catal.*, 2019, **9**(9), 8798–8809.
46 C. Costentin, S. Drouet, G. Passard, M. Robert and J.-M. Savéant, *J. Am. Chem. Soc.*, 2013, **135**(6), 9023–9031.
47 (*a*) R. Matheu, S. Neudeck, F. Meyer, X. Sala and A. Llobet, *ChemSusChem*, 2016, **9**(23), 3361–3369; (*b*) W. C. Hsu and Y. H. Wang, *ChemSusChem*, 2022, **15**(5), e202102378.
48 P. Lepcha, S. Biswas, S. N. Chowdhury, S. Bose, J. Debgupta, S. Paul and A. N. Biswas, *Eur. J. Inorg. Chem.*, 2022, **2023**(26), e202200611.
49 G. Ruan, P. Ghosh, N. Fridman and G. Maayan, *J. Am. Chem. Soc.*, 2021, **143**(28), 10614–10623.
50 P.-G. Barros, D. Moonshiram, M. G. Sepulcre, P. Pelosin, C. G. Suriñach, J. B. Buchholz and A. Llobet, *J. Am. Chem. Soc.*, 2020, **142**(41), 17434–17446.

51 M. K. Coggins, M. T. Zhang, Z. Chen, N. Song and T. J. Meyer, *Angew. Chem., Int. Ed.*, 2014, **53**(45), 12226–12230.
52 J. Wang, Y. Ping, Y. Chen, S. Liu, J. Dong, Z. Ruan, X. Liang and J. Lin, *Dalton Trans.*, 2024, **53**(11), 5222–5229.
53 Q. Q. Hu, X. J. Su and M. T. Zhang, *Inorg. Chem.*, 2018, **57**(17), 10481–10484.
54 (*a*) K. Fujisawa, M. Tanaka, Y. Moro-oka and N. Kitajima, *J. Am. Chem. Soc.*, 1994, **116**(26), 12079–12080; (*b*) P. Chen, D. E. Root, C. Campochiaro, K. Fujisawa and E. I. Solomon, *J. Am. Chem. Soc.*, 2003, **125**(2), 466–474; (*c*) B. Kim and K. D. Karlin, *Acc. Chem. Res.*, 2023, **56**(16), 2197–2212; (*d*) P. K. Hota, A. Jose, S. Panda, E. M. Dunietz, A. E. Herzog, L. Wojcik, N. L. Poul, C. Belle and E. I. Solomon, *J. Am. Chem. Soc.*, 2024, **146**(19), 13066–13082.
55 K. Yu, Y. Sun, D. Zhu, Z. Xu, J. Wang, J. Shen, Q. Zhang and W. Zhao, *Chem. Commun.*, 2022, **58**(92), 12835–12838.
56 D. D. Boer, A. I. Konovalov, M. A. Siegler and D. G. H. Hetterscheid, *Inorg. Chem.*, 2023, **62**(14), 5303–5314.
57 S.-Y. Zhao, X.-L. Zhu, X.-H. Wang, Y.-Y. Cao, Q.-A. Li, S.-Y. Qin, T.-S. Wang and H.-X. Zhang, *Appl. Organomet. Chem.*, 2023, **37**(9), e7198.
58 J. Shen, M. Wang, J. Gao, H. Han, H. Liu and L. Sun, *ChemSusChem*, 2017, **10**(22), 4581–4588.
59 J. Lin, S. Zheng, L. Hong, X. Yang, W. Lv, Y. Li, C. Dai, S. Liu and Z. Ruan, *New J. Chem.*, 2022, **46**(30), 14642–14648.
60 Q. Bai, X. Yang, S. Zheng, L. Hong, C. Dai, L. Lin, P. Wang and X. Liang, *Sustainable Energy Fuels*, 2022, **6**(15), 3643–3648.
61 (*a*) Z. G. Lada, Y. Sanakis, C. P. Raptopoulou, V. Psycharis, S. P. Perlepes and G. Mitrikas, *Dalton, Trans.*, 2017, **46**(26), 8458–8475; (*b*) E. Garibba and G. Micera, *J. Chem. Educ.*, 2006, **83**(8), 1229; (*c*) B. Kozlevčar, *Croat. Chem. Acta*, 2020, **81**(2), 369–379; (*d*) P. K. Hota, A. Jose, S. Panda, E. M. Dunietz, A. E. Herzog, L. Wojcik, N. L. Poul, C. Belle, E. I. Solomon and K. D. Karlin, *J. Am. Chem. Soc.*, 2024, **146**(19), 13066–13082; (*e*) S. Kakuda, R. L. Peterson, K. Ohkubo, K. D. Karlin and S. Fukuzumi, *J. Am. Chem. Soc.*, 2013, **135**, 6513–6522.
62 W. Kohn and L. J. Sham, *Phys. Rev. [Sect.] A*, 1965, **140**(4), A1133–A1138.
63 P. Hohenberg and W. Kohn, *Phys. Rev. [Sect.] B*, 1964, **136**(3), B864–B871.
64 M. J. Frisch, G. W. Trucks, H. B. Schlegel, G. E. Scuseria, M. A. Robb, J. R. Cheeseman, G. Scalmani, V. Barone, G. A. Petersson, H. Nakatsuji, X. Li, M. Caricato, A. V. Marenich, J. Bloino, B. G. Janesko, R. Gomperts, B. Mennucci, H. P. Hratchian, J. V. Ortiz, A. F. Izmaylov, J. L. Sonnenberg, D. W. -Young, F. Ding, F. Lipparini, F. Egidi, J. Goings, B. Peng, A. Petrone, T. Henderson, D. Ranasinghe, V. G. Zakrzewski, J. Gao, N. Rega, G. Zheng, W. Liang, M. Hada, M. Ehara, K. Toyota, R. Fukuda, J. Hasegawa, M. Ishida, T. Nakajima, Y. Honda, O. Kitao, H. Nakai, T. Vreven, K. Throssell, J. A. J. Montgomery, J. E. Peralta, F. Ogliaro, M. J. Bearpark, J. J. Heyd, E. N. Brothers, K. N. Kudin, V. N. Staroverov, T. A. Keith, R. Kobayashi, J. Normand, K. Raghavachari, A. P. Rendell, J. C. Burant, S. S. Iyengar, J. Tomasi, M. Cossi, J. M. Millam, M. Klene, C. Adamo, R. Cammi, J. W. Ochterski, R. L. Martin, K. Morokuma, O. Farkas, J. B. Foresman and D. J. Fox, *Gaussian 16, Revision C.01*, Gaussian, Inc., Wallingford CT, 2016.
65 A. D. Becke, *Phys. Rev. A:At., Mol., Opt. Phys.*, 1988, **38**(6), 3098–3100.
66 C. Lee, W. Yang and R. G. Parr, *Phys. Rev. B:Condens. Matter Mater. Phys.*, 1988, **37**(2), 785–789.
67 W. J. Hehre, R. Ditchfield and J. Pople, *J. Chem. Phys.*, 1972, **56**, 2257–2261.
68 L. E. Roy, P. J. Hay and R. L. Martin, *J. Chem. Theory Comput.*, 2008, **4**(7), 1029–1031.
69 J. K. Nørskov, J. Rossmeisl, A. Logadottir, L. Lindqvist, J. R. Kitchin, T. Bligaard and H. Jónsson, *J. Phys. Chem. B*, 2004, **108**(46), 17886–17892.
70 M. J. Craig, G. Coulter, E. Dolan, J. S. -López, E. M. -Torres, W. Schmitt and M. G. -Melchor, *Nat. Commun.*, 2019, **10**(1), 4993.
71 (*a*) D. Raj and S. K. Padhi, CSD Communication, 2024, DOI: DOI: **10.5517/ccdc.csd.cc2lkxkn**, CCDC 2400502; (*b*) M. Raj and S. K. Padhi, CSD Communication, 2024, DOI: DOI: **10.5517/ccdc.csd.cc2lkxlp**, CCDC 2400503.